

Evidence for multiple Ferrel-like cells on Jupiter

Keren Duer^{1*}, Nimrod Gavriel^{1*}, Eli Galanti¹, Yohai Kaspi¹,
 Leigh N. Fletcher², Tristan Guillot³, Scott J. Bolton⁴, Steven M. Levin⁵,
 Sushil K. Atreya⁶, Davide Grassi⁷, Andrew P. Ingersoll⁸, Cheng Li⁶, Liming Li⁹,
 Jonathan I. Lunine¹⁰, Glenn S. Orton⁵, Fabiano A. Oyafuso⁵, J. Hunter Waite, Jr.⁴

October 15, 2021

¹*Department of Earth and Planetary Sciences, Weizmann Institute of Science, Rehovot, Israel*

²*School of Physics and Astronomy, University of Leicester, University Road, Leicester, LE1 7RH, UK*

³*Universit  Cote d'Azur, OCA, Lagrange CNRS, 06304 Nice, France*

⁴*Southwest Research Institute, San Antonio, Texas, TX, USA*

⁵*Jet Propulsion Laboratory, California Institute of Technology, 4800 Oak Grove Drive, Pasadena, CA 91109, USA*

⁶*Department of Climate and Space Sciences and Engineering, University of Michigan, Ann Arbor, MI, USA*

⁷*Istituto di Astrofisica e Planetologia Spaziali, INAF, Rome, Italy*

⁸*California Institute of Technology, Pasadena, California, USA*

⁹*University of Houston, Houston, TX, USA*

¹⁰*Department of Astronomy, Cornell University, Ithaca, New York 14853, USA*

* These authors contributed equally to this work

Key points

- Measurements from multiple instruments of the Juno mission are interpreted to reveal the meridional circulation beneath Jupiter's clouds
- 16 Jet-paired deep cells, extending to at least 240 bar, are revealed between latitudes 60°S and 60°N, driven by turbulence similar to Earth's Ferrel cells
- The findings are supported by modeling the advection of tracers due to the cells, showing agreement with NH₃ data

Abstract

Jupiter's atmosphere is dominated by multiple jet streams which are strongly tied to its 3D atmospheric circulation. Lacking a rigid bottom boundary, several models exist for how the meridional circulation extends into the planetary interior. Here we show, collecting evidence from multiple instruments of the Juno mission, the existence of mid-latitude meridional circulation cells which are driven by turbulence, similar to the Ferrel cells on Earth. Different than Earth, which contains only one such cell in each hemisphere, the larger, faster rotating Jupiter can incorporate multiple cells. The cells form regions of upwelling and downwelling, which we show are clearly evident in Juno's microwave data between latitudes 60°S and 60°N. The existence of these cells is confirmed by reproducing the ammonia observations using a simplistic model. This study solves a long-standing puzzle regarding the nature of Jupiter's sub-cloud dynamics and provides evidence for 8 cells in each Jovian hemisphere.

Plain Language Summary

The cloud layer of Jupiter is divided into dark and bright bands that are shaped by strong east-west winds. Such winds in planetary atmospheres are thought to be tied with a meridional circulation. The Juno mission collected measurements of Jupiter’s atmosphere at various wavelengths, which penetrate the cloud cover. Here we provide evidence, using the Juno data, of 8 deep Jovian circulation cells in each hemisphere encompassing the east-west winds, gaining energy from atmospheric waves, and extending at least to a depth of hundreds of kilometers. Different than Earth, which has only 1 analogous cell in each hemisphere, known as a Ferrel cell, Jupiter can contain more cells due to its larger size and faster spin. To support the presented evidence, we modeled how ammonia gas would spread under the influence of such cells and compared it to the Juno measurements. The presented results shed light on the unseen flow structure beneath Jupiter’s clouds.

1 Introduction

Over the last few decades, spacecraft and ground-based observations have gathered data about Jupiter’s atmosphere, including measurements of cloud reflectance (García-Melendo and Sánchez-Lavega, 2001), winds (Porco et al., 2003; Salyk et al., 2006; Tollefson et al., 2017), composition (Taylor et al., 2004) and lightning flashes (Little et al., 1999). Since 2016, the Juno spacecraft has provided unprecedented measurements that revealed new information on the deep dynamics of Jupiter (Bolton et al., 2017). Gravity science enabled an accurate mapping of Jupiter’s gravitational field (Iess et al., 2018), resulting in the inference that the zonal jets penetrate ~ 3000 km deep (Kaspi et al., 2018; Guillot et al., 2018), where they possibly decay due to magnetic drag (Liu et al., 2008; Dietrich and Jones, 2018; Kaspi et al., 2020) and may also require the presence of a stable layer (Christensen et al., 2020). The Jovian Infrared Auroral Mapper (JIRAM) provided measurements of tropospheric species distribution below the cloud level (Grassi et al., 2020). The Microwave Radiometer (MWR) measurements, inferred as brightness temperature (T_b), revealed the deep ammonia abundance (Li et al., 2017; Oyafuso et al., 2020), as well as lightning at a frequency of 600 MHz (Brown et al., 2018). The combination of these observations allows the essential nature of Jupiter’s deep overturning circulation to be revealed, as the flows associated with such circulation are directly related to cloud formation, temperature variations, lightning occurrences, tracer distributions and turbulence.

Earth’s atmosphere is commonly referred to as possessing a three-cell meridional structure in each hemisphere (Vallis, 2017), which can be recognized in the zonal-averaged velocities. Circulation cells of such nature are thought to prevail in the atmospheres of terrestrial planets (Read et al., 2018) and were observed, for example, on Mars (Lewis et al., 2007) and Venus (Limaye, 2007). On the terrestrial planets, the solid surface drag plays a part in maintaining the circulation in the cells. However, as the giant planets hold no such surface, the mere possibility of them possessing meridional circulation cells remained uncertain. Earth’s midlatitudes are governed by the Ferrel cells, which are driven by atmospheric turbulence, creating regions of eddy momentum flux convergence at midlatitudes (Vallis, 2017). These cells accompany the midlatitude jets and are connected to the cloud structure in Earth’s atmosphere.

The prominent banded structure at the cloud tops of Jupiter’s atmosphere (Fig. 1a) has been observed for centuries (Vasavada and Showman, 2005). These reflectivity contrasts are partially aligned (mainly at low latitudes, Ingersoll et al. (2000)) with the belts and zones (Fig. 1a), defined by the sign of the zonal-wind vorticity ($\bar{\zeta} = -\partial \bar{u} / \partial y$ in Fig. 1c, where u is zonal velocity, y is in the meridional direction and an over-line represents a zonal mean). Voyager measurements suggested that the zones are associated with ascending motion, but this was limited to low latitudes due to its equatorial trajectory and to altitudes above 0.5 bar (Gierasch et al., 1986). The latitudinal profile of the zonal wind, calculated using cloud-tracking (García-Melendo and Sánchez-Lavega, 2001; Porco et al., 2003; Tollefson et al., 2017), reveals that the equatorial region is characterized by a strong eastward flow, while the midlatitudes exhibit alternating jets, spaced $2 - 8^\circ$ apart in latitude (Fig. 1b). The midlatitude jets are correlated with the eddy momentum flux convergence (Salyk et al., 2006) ($-\partial(u'v')/\partial y$ in Fig. 1d, where v is meridional velocity and an apostrophe represents deviations from the zonal mean, i.e. “eddy” terms), implying that the midlatitude jets are eddy-driven (Ingersoll et al., 2000; Young and Read, 2017), similar to the jets within Earth’s Ferrel cells (Schneider, 2006; Vallis, 2017). To illustrate the relation between the jets and the eddies, regions of positive (negative) vorticity gradient, $\partial \zeta / \partial y = -\partial^2 \bar{u} / \partial y^2$, at midlatitudes, are marked by light red (blue) bands (Fig. 1), where counter-clockwise (clockwise) Ferrel-like circulation cells are expected in the northern hemisphere (NH). Similar circulations, but in opposite directions, apply for the southern hemisphere (SH). Evidence for vertical motion comes also from observations of lightning flashes (Little et al., 1999; Porco et al., 2003; Brown et al., 2018), suggesting updrafts in cyclonic belt regions (e.g., Fig. 1e).

Additional information regarding Jupiter’s deep atmosphere can be obtained by probing Jupiter’s interior at

microwave frequencies. Juno’s MWR has 6 microwave channels (Janssen et al., 2017), each measuring the atmospheric T_b at a different depth (Janssen et al., 2017; Bolton et al., 2017; Oyafuso et al., 2020; Fletcher et al., 2021), and collectively covering the range between ~ 0.7 and ~ 240 bar (Fig. 1g,h, see also supporting information - SI). T_b measurements are affected by both ammonia abundance and temperature [and water in the case of the longest wavelengths, Li et al. (2017, 2020); Fletcher et al. (2021)]. If the latitudinal gradients of T_b were primarily driven by temperature changes, then thermal wind balance implies that the midlatitude jets strengthen from the cloud-deck to about ~ 8 bar, and then decay slowly towards the interior (Fletcher et al., 2021). However, interpreting T_b as temperature would also imply that the equatorial wind double its magnitude below the cloud level (Bolton et al., 2017), which is inconsistent with gravity constraints (Duer et al., 2020). Thus, the latitudinal variation of T_b is probably governed by ammonia opacity, resulting in a map of ammonia abundance (Li et al., 2017), and implying that the zonal winds are nearly barotropic (Fletcher et al., 2021). The overall ammonia structure, supported also by earlier observations (de Pater et al., 2001), reveals stratification of ammonia with depth, although the mean ammonia profile changes the sign of its vertical gradient at the $\sim 2 - 8$ bar region (Giles et al., 2017; Li et al., 2017; de Pater et al., 2019). The atmospheric depletion and stratification of ammonia is likely linked to small-scale storm activity (Guillot et al., 2020a,b), where water-ammonia hail, forming around the 1-bar level, falls below the water-cloud base and releases ammonia and water at altitudes below 10 bar (Guillot et al., 2020b). Additional measurements of ammonia come from Juno’s JIRAM, which evaluated the ammonia distribution at a depth of $\sim 5 - 6$ bar (Grassi et al., 2010, 2020) (Fig. 1f), indicating, as the MWR measurements, that ammonia varies with latitude. These variations are the key observation for this study, as ammonia anomalies (deviations from the isobaric mean) can reveal details about Jupiter’s overturning circulation (Ingersoll et al., 2017; Fletcher et al., 2021; Lee and Kaspi, 2021).

2 Ammonia anomalies due to vertical advection

In the presence of a stable vertical ammonia concentration gradient, advection by the vertical branches of a meridional circulation can affect the concentration distribution, potentially leading to steady anomalies. Therefore, the wavy structure of Jupiter’s ammonia distribution (Fig. 1f-h) can be explained by the presence of meridional circulation cells. On Jupiter, as condensation of ammonia is expected only at the upper levels of the atmosphere ($0.5 - 1$ bar), the ammonia concentration at those levels should be lower than at depth (Fletcher et al., 2020). In addition, precipitation, small-scale turbulence, thermochemical and chemical reactions, and diffusion are also expected to determine the vertical ammonia distribution (M_a) (Guillot et al., 2020b). The M_a profile estimated from the MWR (Li et al., 2017) reveals a local minimum at ~ 6 bar (Fig. 2a). This profile is used in this study as the background state, to explain the ammonia anomalies.

Here, we focus on two regions with distinctly different deep dynamics: the equatorial region (planetocentric latitudes 20°S to 20°N), where superrotation is assumed to be fueled by eddy momentum fluxes perpendicular to the spin axis (e.g., Busse, 2002), and midlatitudes (60°S to 20°S and 20°N to 60°N), where alternating jets are postulated to be driven by horizontal eddies associated with mass-transporting meridional cells (e.g., Salyk et al., 2006; Schneider and Liu, 2009; Young et al., 2019).

We begin with the midlatitudes, where the meridional cells are mechanically driven (see below) by turbulence, similar to Earth’s Ferrel cells, which form as a consequence of atmospheric waves breaking in midlatitudes (Vallis, 2017). Unlike the largely baroclinic midlatitudes of Earth, which result in mostly non-mass-transporting Ferrel cells (Jukes, 2001; Vallis, 2017), the predominantly barotropic flows on Jupiter (at the depth range associated with the MWR measurements) (Kaspi et al., 2018; Kaspi et al., 2020; Galanti and Kaspi, 2021) may allow mass-transporting meridional cells (see SI). Consistently, deep convection models of Jupiter also show barotropic flows (e.g., Busse, 1976; Aurnou and Olson, 2001). The upper branch of Earth’s Ferrel cells consists of a balance between the Coriolis force and the eddy momentum flux convergence,

$$-f\bar{v} = -\frac{\partial \left(\overline{u'v'} \right)}{\partial y}, \quad (1)$$

where f is the Coriolis parameter. This upper branch balance, which is the leading order balance of the steady state zonal mean zonal momentum equation, is expected to hold within the equivalent cells on Jupiter (see SI). This balance can hold down to a depth of only a few bars, as inferred from energy considerations (Liu and Schneider, 2010), implying flows from belts to zones within the cloud layer of the Jovian atmosphere. In the lower branch of the terrestrial Ferrel cells, the balance is between the Coriolis force and a surface drag (Vallis, 2017). Since the Jovian atmosphere lacks a bottom solid boundary, surface drag cannot act to oppose the Coriolis force, although

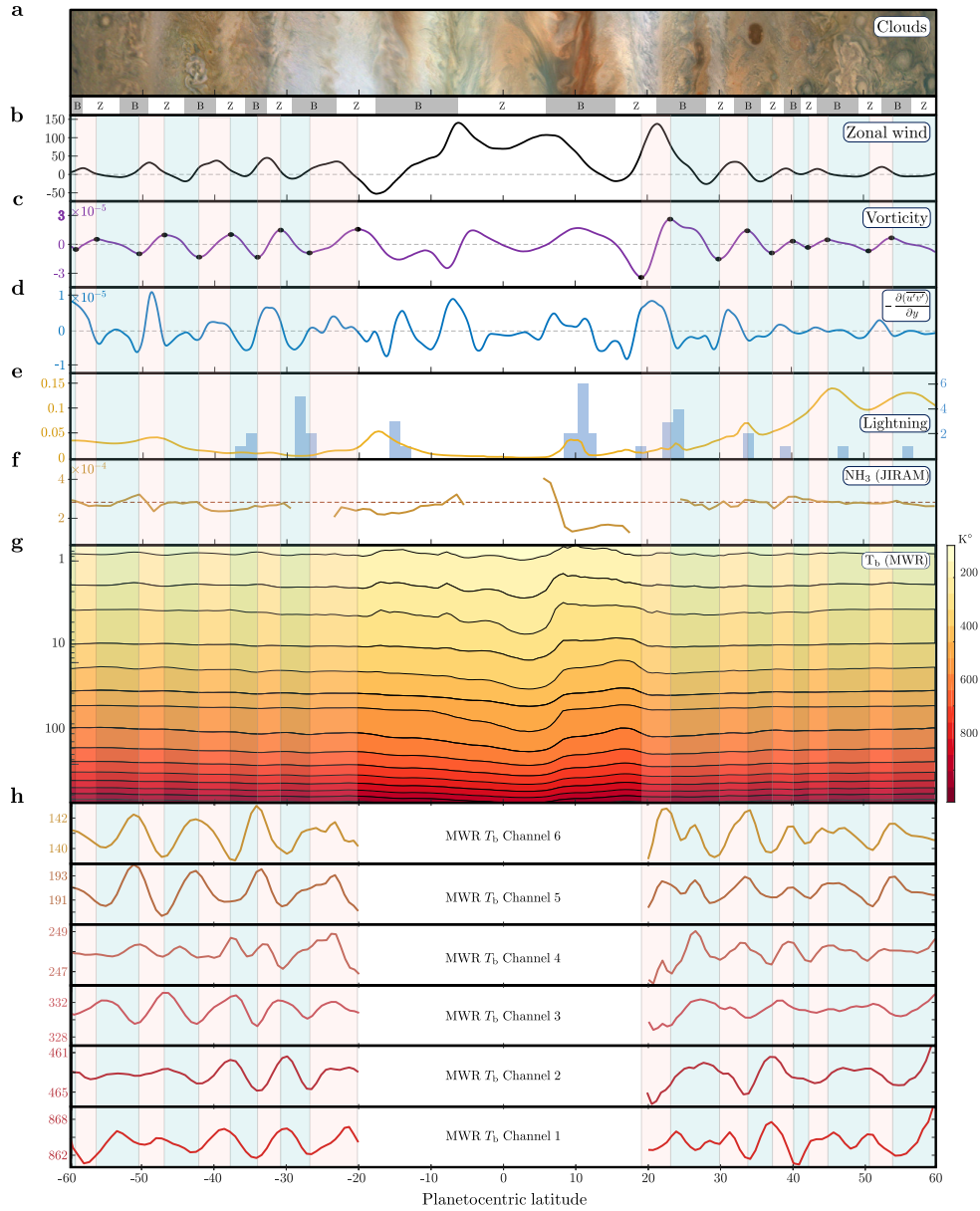


Figure 1: Observations of Jupiter’s atmosphere. (a) Image of Jupiter’s clouds (longitudes $69 - 87^\circ$) taken by JunoCam on Dec. 26th 2019 during perijove 24 (image credit: NASA/JPL/SwRI/MSSS/Gerald Eichstaedt/John Rogers), with the traditional “dark” belts (“bright” zones) defined as regions of cyclonic (anticyclonic) vorticity, identified below as ‘B’ (‘Z’). (b) Jupiter’s zonally averaged zonal wind [$\pm 15 \text{ m s}^{-1}$] measured by the Hubble space telescope on December 11, 2016, during Juno’s third perijove (Tollefson et al., 2017). (c) The zonally averaged vorticity [s^{-1}], calculated from the zonal wind profile (panel b). Black dots represent local extrema in the midlatitudes. (d) Eddy momentum flux convergence [$\pm 2 \times 10^{-6} \text{ m s}^{-2}$] calculated from 58 image pairs taken by Cassini during its Jupiter flyby in December, 2000 (Salyk et al., 2006). (e) Lightning detections [s^{-1}] by Juno’s MWR during perijoves 1-8 (yellow, left axis, Brown et al., 2018) and number of lightning storms detected by the Cassini during its flyby (blue, right axis, Porco et al., 2003). (f) Distribution of ammonia [volume mixing ratio] and its mean (dashed) at a depth of ~ 6 bar, measured by Juno’s JIRAM during perijoves 1-15 (Grassi et al., 2020). (g) Nadir T_b [$^\circ\text{K}$] (color) interpolated between pressure levels of 0.7 and 240 bar (vertical axis), measured by Juno’s MWR during perijoves 1-12 (Oyafuso et al., 2020). (h) Reconstructed MWR Brightness temperature at midlatitudes. A frequency filter is applied according to Eq. S7. The standard deviation of each channel and latitude is available in Fig. S3 and Fig. S4. It can be seen that T_b changes its trend at the borders between cells, consistent with the Ferrel-like cells hypothesis. (b-h) Light red (blue) bands in the midlatitudes indicate regions of positive (negative) vorticity gradients.

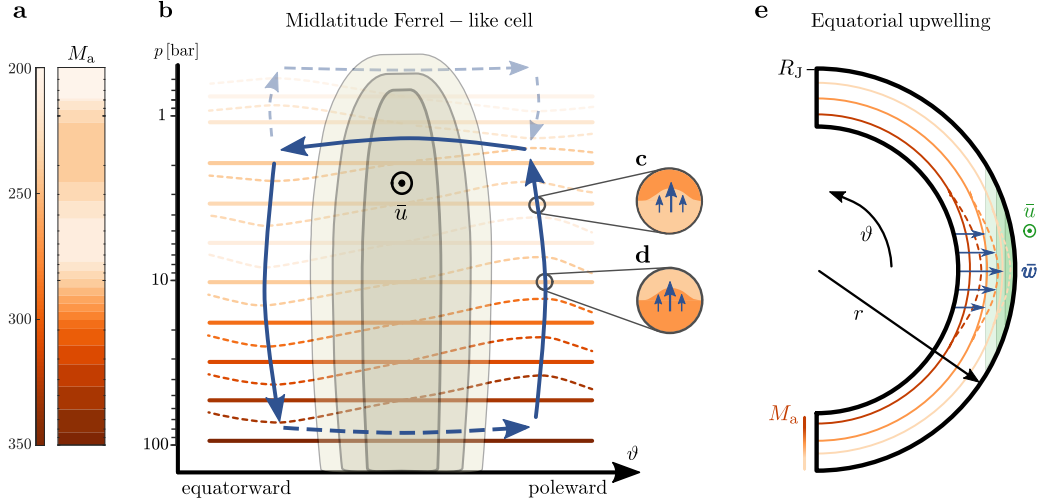


Figure 2: Schematics of Jupiter’s meridional circulation as inferred from the ammonia distribution. (a) The vertical structure of the meridionally averaged ammonia concentration (M_a) [ppm], as interpreted from the T_b data (Li et al., 2017). (b) Illustration of a midlatitude Ferrel-like circulation cell (blue arrows) in the NH, looking from east towards the west. The cells are accompanied by an eddy-driven barotropic jet (\bar{u}), which peaks at the center of the cell (beige contours). Ammonia constant-concentration lines are illustrated with orange shades (according to the ammonia vertical profile from panel a). Dashed orange lines are deviations from M_a , driven by vertical advection. The return flow of the cell, illustrated by a dashed blue arrow, lies at an unknown depth. An oppositely directed upper cell, as suggested by pre-Juno measurements (Ingersoll et al., 2000; Showman and de Pater, 2005; Fletcher et al., 2020), is demonstrated by dashed transparent arrows. (c) A closer look at the region where the rising air advects ammonia-poor fluid to an ammonia-rich layer, associated with pressure levels between 1.5 and 6 bar. (d) Here, rising gas drags higher ammonia concentration to a lower ammonia concentration region, associated with pressure levels deeper than 6 bar. (e) A cross section of Jupiter’s equatorial upwelling (\bar{w}), associated with a superrotating jet (\bar{u} , green contours), leading to ammonia concentration maximum. The equatorial M_a (orange contours) is assumed to decrease with radius (Fig. S8). R_J is Jupiter’s radius and ϑ and r are the latitudinal and radial directions, respectively.

it has been suggested that if the cells extend as deep as the jets (Kaspi et al., 2020), the Lorentz force can act as a magnetic drag (Liu et al., 2008; Liu and Schneider, 2010; Wicht et al., 2019). Another possible mechanism that allows the jets to be barotropic in the upper atmosphere and decay in the interior is the presence of a stable layer, as was shown lately in several studies (Debras and Chabrier, 2019; Christensen et al., 2020; Wicht and Gastine, 2020).

The direction of each Ferrel-like cell corresponds to the direction of the respective midlatitude jet. Eastward (westward) jets are located in cells of eastward momentum flux convergence (divergence) implying (Eq. 1) a counterclockwise (clockwise) circulation in the NH, and a clockwise (counterclockwise) circulation in the SH (Fig. 1b,d). The upper branch of the Ferrel-like cells may coincide with the lower branch of stacked upper cells with an opposite circulation (Ingersoll et al., 2000; Showman and de Pater, 2005) (dashed transparent lines in Fig. 2b), and therefore may share the same balance (Eq. 1). Indications for the upper cells come from temperature and shallow tracer distributions (Gierasch et al., 1986; Fletcher et al., 2016; de Pater et al., 2019). Similar to the balance describing the deeper branch of the lower cells, the upper branch of the upper cells requires a drag force, which may result from breaking of atmospheric waves (Gierasch et al., 1986; Ingersoll et al., 2021).

The background ammonia profile is skewed by the vertical branches of the cells (dashed orange lines in Fig. 2b), maximizing the ammonia meridional gradient where the jet velocity peaks (i.e., in the middle of the cell). This means that a correlation (along isobars) is expected between the zonal jets and the meridional gradient of the ammonia concentration at midlatitudes (Duer et al., 2020; Fletcher et al., 2021). However, since the vertical gradient of M_a changes with depth (Li et al., 2017) (Fig. 2a), the nature of the correlation should change as well, as illustrated in Fig. 2c,d. These simple considerations motivate the examination of the correlation between \bar{u} and $\partial_y m_a$ ($-\partial_y T_b$) in midlatitudes (Fig. 3a,c, also see SI). Note that T_b corresponds inversely to ammonia abundance at a certain pressure level (Li et al., 2017). For a deep-wind estimate, we use the measured cloud-level winds (Tollefson et al., 2017) projected inward in a direction parallel to the axis of rotation, without any change in magnitude (in the

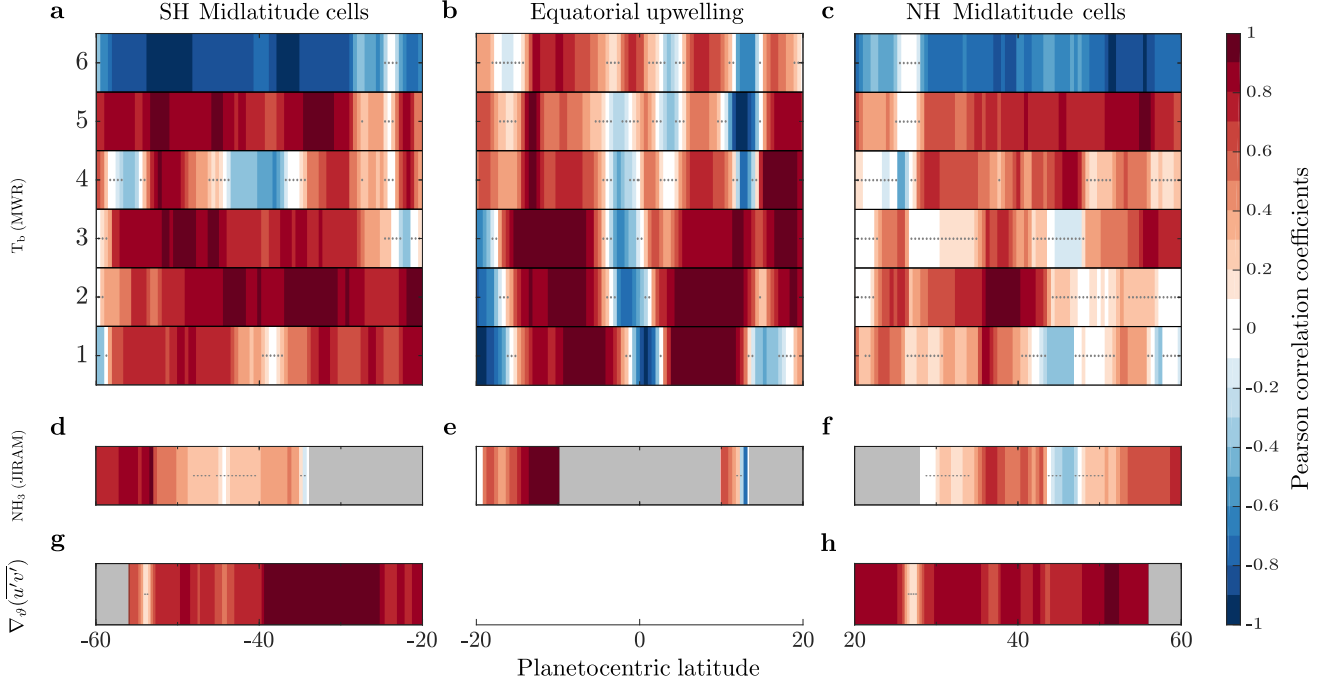


Figure 3: Pearson correlation coefficients as a function of latitude. The correlations exemplify the relations presented in Fig. 2. (a) and (c), correlations calculated between the zonal jets (\bar{u}) and the T_b meridional gradients ($\partial_y T_b$), adjusted by the sign of the vertical gradient of M_a , in the six MWR channels, for the SH and NH, respectively. (b) Correlations computed between the zonal jet velocity and T_b ($\bar{u} \propto -T_b$). (d) and (f), Correlations between the zonal velocity and the ammonia abundance gradients ($\partial_y \text{NH}_3$), measured by JIRAM, in the SH and NH, respectively. (e) Correlations between the zonal velocity and the ammonia abundance from JIRAM ($\bar{u} \propto \text{NH}_3$). (g) and (h) Correlations between the zonal velocity and the eddy momentum flux convergence ($\bar{u} \propto -\partial_y (\overline{u'v'})$), in the SH and NH, respectively. Gray dots represent correlations that are not statistically significant (confidence level 95%) and gray regions show where measurements were not available. No data is available for the eddy fluxes in the equatorial region, as evaluating them requires measurements of the vertical winds (see SI), which are yet to be achieved.

upper 240 bar), as implied by gravity measurement constraints (Galanti and Kaspi, 2021; Galanti et al., 2021). The correlations are performed using a 4° latitudinal bin (see SI). By this, the suggested correlations in Fig. 2 can be tested locally, rather than over an entire hemisphere (Duer et al., 2020; Fletcher et al., 2021).

At midlatitudes the overall positive correlations for MWR channels 1-5 indicate the existence of Ferrel-like cells at depths between 1.5 and 240 bar (Fig. 3a,c). The positive correlation with ammonia estimates by JIRAM (Fig. 3d,f) further strengthens the prominence of the proposed cells. Channel 6 (~ 0.7 bar) exhibits negative correlations in midlatitudes (Fig. 3a,c), implying that the deep cells do not extend higher than ~ 1 bar, and support the existence of counter-rotating cells above that level (Ingersoll et al., 2000; Showman and de Pater, 2005; Fletcher et al., 2020). To verify that the relation shown in Eq. 1 holds in the cells as illustrated in Fig. 2b, regional correlations between \bar{u} and $-\partial_y (\overline{u'v'})$ are shown for midlatitudes (Fig. 3g,h). This positive correlation further strengthens the existence of the Ferrel-like cells, where converging eddy momentum fluxes are the source of momentum. Overall, the correlation analysis reveals multiple deep Ferrel-like cells, extending from ~ 1 bar to at least 240 bar.

The equatorial region of Jupiter, characterized by a wide eastward jet, needs to be treated differently. Gravity analysis reveals that Jupiter’s interior (deeper than ~ 3000 km) is rotating as a rigid body (Guillot et al., 2018). Extending the zonal wind along the direction of the spin axis thus separates the equatorial region (17° S to 17° N) from the truncated cells at midlatitudes (see SI). The superrotating wind at low latitudes requires a source of momentum (Imamura et al., 2020). Theories for such sources include meridional (Potter et al., 2014; Laraia and Schneider, 2015) and vertical (Aurnou and Olson, 2001; Busse, 2002; Christensen, 2002; Heimpel et al., 2005; Kaspi et al., 2009; Dietrich and Jones, 2018), propagation of waves. For the vertical case, several studies have shown that an equatorial superrotation in giant planets can be driven by eddy momentum fluxes perpendicular to the axis of rotation (Heimpel et al., 2005; Kaspi et al., 2009; Gastine et al., 2014). These fluxes transfer momentum outwards and lead to a mean upwelling at the equatorial region (see SI). Such an upwelling should lead to a maximum concentration anomaly of any stably stratified matter (Fig. 2e). In the equatorial region, the minimum in M_a around ~ 6 bar nearly vanishes (Fig. S8), suggesting that the positive ammonia anomalies at the equatorial region (Fig. S2a) are due to the upwelling from deep. To examine this, at the equator, the correlation is calculated between the zonal velocity (\bar{u}) and the ammonia concentration itself ($-T_b$ for the MWR or NH_3 for the JIRAM measurements). Using a regional correlation analysis (see SI), it is apparent that the correlations are largely positive at all depths (Fig. 3b,e), implying that an equatorial upwelling is dominant from the cloud deck and down to at least 240 bar. Very close to the equator, the correlation is negative due to the local minimum in the zonal velocity (Fig. 1b).

3 Model reconstruction of Jupiter’s ammonia distribution

To further validate that the positive correlations shown in Fig. 3a,c are indeed due to the existence of meridional circulation cells, we reconstruct the measured variations using a simplified advection-relaxation model. Beginning with a steady-state zonal-mean conservation of species equation for ammonia, assuming that diffusion terms are small, the leading-order balance is

$$\bar{w}(\vartheta, r) \frac{\partial m_a(\vartheta, r)}{\partial r} + \bar{v}(\vartheta, r) \frac{\partial m_a(\vartheta, r)}{r \partial \vartheta} = -G(r) (m_a(\vartheta, r) - M_a(r)), \quad (2)$$

where \bar{w} is the zonally averaged radial velocity, and m_a , the variable solved for by the model, is the (zonal-mean) molar fraction of ammonia. M_a is the ammonia concentration averaged over isobaric surfaces (Fig. 2a), and G is the inverse of a Newtonian relaxation timescale. The two terms on the left-hand side represent advection by the mean circulation, and the right-hand side term is a source term parameterized as a simple Newtonian relaxation of ammonia. This relaxation term is assumed to include all the processes resulting in the observed M_a as it acts against local anomalies toward this mean vertical structure. To qualitatively illustrate how the Ferrel-like cells’ footprint might appear in the ammonia distribution map (m_a), we solve the advection-relaxation balance shown in Eq. 2, for the midlatitudes between 1.5 and 240 bar (see SI). As the balance in Eq. 2 indicates, it is assumed that the relaxation time scale (G^{-1}) is such that the advection and relaxation terms balance each other.

The zonally averaged velocity components (\bar{v} , \bar{w}) of the circulation cells, necessary for setting the advection terms of Eq. 2, can be projected from the available wind data according to the outline illustrated in Fig. 2b. Specifically, we relate between the circulation cells and the wind data corresponding to the following assumptions (see also SI). The borders between the cells are set at local extrema of the observed cloud-level vorticity, the directions of the circulation cells are set according to the directions of the jets in the middle of each cell, and the strength of the circulation in each cell is set by the measured eddy momentum flux convergence along the cell (Fig. S5). As the three terms in Eq. 2 should be proportional, but cannot be uniquely determined, the values of \bar{w} , \bar{v} and G are

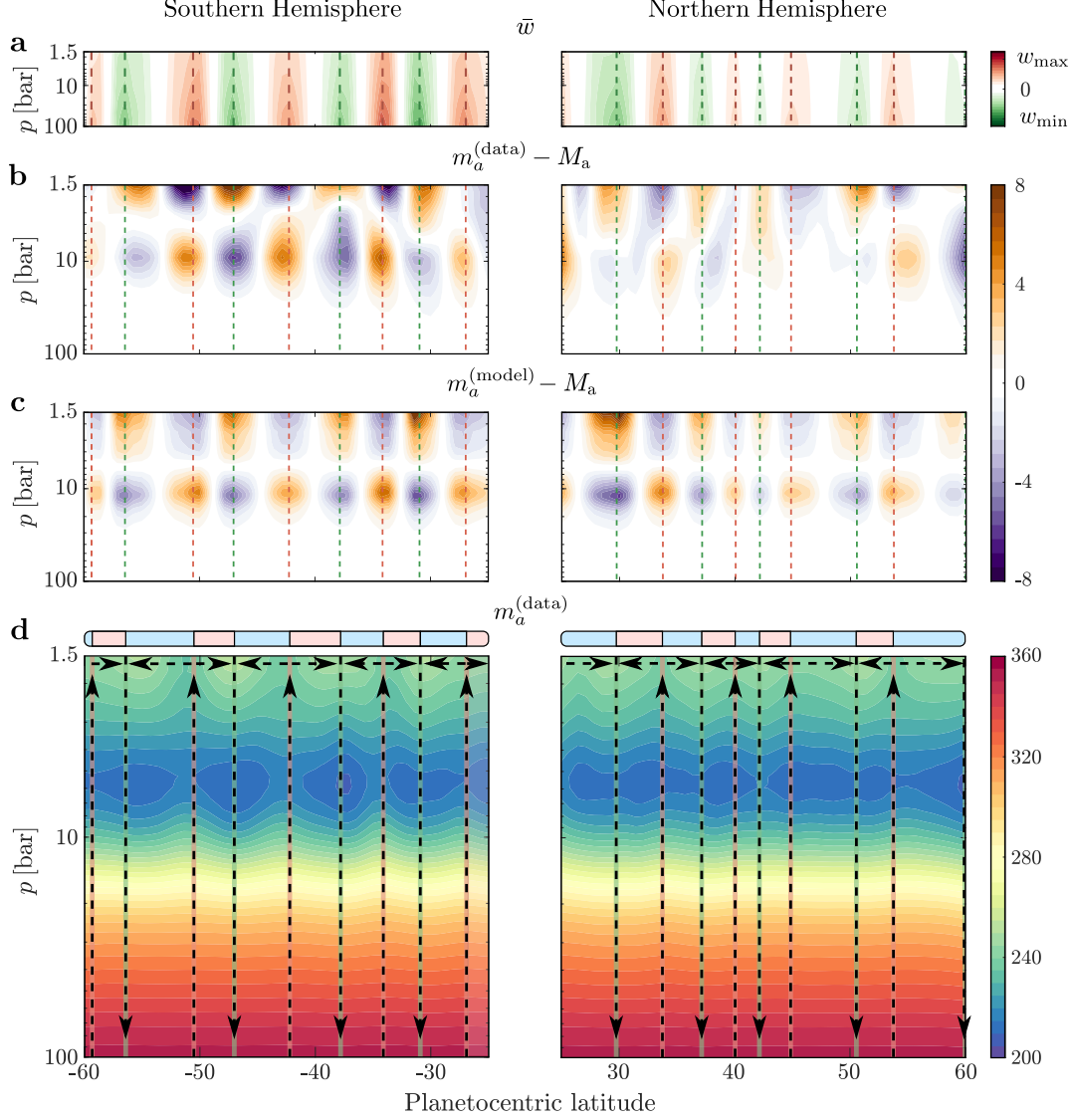


Figure 4: Jupiter’s Ammonia distribution driven by an array of circulation cells. (a) The normalized vertical zonal-mean wind (\bar{w}), as a function of latitude and pressure, used in the model. Red and green contours are upward and downward winds, respectively. (b) The ammonia anomalies reconstructed from the data [ppm]. Here the vertical mean profile M_a is removed from the ammonia map m_a . (c) The ammonia anomalies [ppm] produced by the advection-relaxation model. (d) The full reconstructed ammonia map $m_a^{(\text{data})}$ [ppm]. Arrows represent the direction of the cells’ vertical and meridional winds. (a-d) Red and green vertical lines are the locations of the upward and downward branches of the cells, respectively. For reference, light red (blue) bands indicate regions of positive (negative) vorticity gradient as in Fig. 1. The vertical axis is truncated at 100 bar as M_a becomes largely uniform beyond this depth, thereby suppressing footprints of advection.

normalized (Fig. 4a). This normalization means that while the model cannot produce absolute values of winds due to unmeasured quantities, it can predict qualitatively how these velocities would be structured spatially and what should be their relative magnitudes, which are sufficient for assessing the existence of the cells. Using scaling arguments, the value of Jupiter’s static stability has recently been estimated to be in the order of 10^{-2} s^{-1} (Lee and Kaspi, 2021), which can provide a further step towards estimating the magnitude of the velocities in the cells.

The described wind scheme results in upwellings (downwellings) on the poleward (equatorward) sides of eastward jets (Fig. 4a). The cells are reversed for westward jets. Finally, as a benchmark for the model results, derivation of the ammonia abundance ($m_a^{(\text{data})}$) from the measured T_b between the latitudes 60°S and 60°N is implemented (see SI, Fig. S2). As the depth of the cells, the width of their branches and the parameter G are unknown, an optimization procedure is performed for determining these parameters to best match the data (see SI). To ensure that this procedure does not influence the qualitative nature of the results, Eq. 2 is also solved with a predefined physically-oriented set of parameters (Figs. S6 and S7).

Using the above assumptions, we solve Eq. 2 to predict the ammonia map ($m_a^{(\text{model})}$), and compare it to $m_a^{(\text{data})}$ (Fig. 4). We stress that the latitudinal variations appearing in the results (Fig. 4c), stem only from the cloud-level wind observations without any assumption on the meridional ammonia variation. For a clear comparison between the $m_a^{(\text{data})}$ and $m_a^{(\text{model})}$, M_a is subtracted from both, such that only anomalies are visible (Fig. 4b,c). Around 10 bar (Fig. 4b), where M_a greatly increases with depth, enriched (depleted) ammonia anomalies appear where upwellings (downwellings) are expected (Fig. 4a). These features flip sign around the 6-bar level, where M_a decreases with depth. These elements are captured well by the advection-relaxation model (Fig. 4c). In the SH, all 18 anomalies apparent in the observations have a counterpart of similar sign, shape and position in the model results, suggesting the existence of 8 meridional circulation cells. This agreement validates that advection by the vertical branches of the cells is the main contributor in the creation of the observed ammonia anomalies. In the NH, similar results are achieved, although the cells are slightly less coherent, perhaps due to unexplained differences between the perijoves in the NH midlatitudes [Fig. S3, Oyafuso et al. (2020); Fletcher et al. (2021)], which might mask the cells’ footprints in the MWR data. Nevertheless, the lightning data reinforces the existence of the NH cells, as lightning peaks are aligned with the rising branch of the cells at the poleward side of the eastward jets (Fig. 1e, Fig. S1), which combined with the MWR data (Fig. 4b-d) provide indication for 8 northern cells. Additional NH centered perijoves during the Juno extended mission may provide data to better constrain the NH cells. For more intuition, one can look at the full ammonia map (Fig. 4d), where iso-concentration lines are pulled up and down by the vertical winds (as schematically illustrated in Fig. 2b), emphasizing the locations of the 16 eddy-driven cells evident in the MWR data.

4 Discussion

The identified array of alternating cells in midlatitudes, along with the equatorial upwelling, are key features in the meridional overturning circulation of the Jovian atmosphere (Fig. 5). The cell’s depth that can be inferred from the MWR measurements is limited to the sensing range (~ 240 bar), and while the midlatitudinal cells are mechanically driven, as the Ferrel cells in Earth’s troposphere, they are likely to extend deeper into the planet, as suggested by multiple theoretical studies (e.g., Liu and Schneider, 2010; Christensen et al., 2020). Similarly, deep meridional cells, which are mechanically driven, have been suggested to exist on the Sun (Miesch and Hindman, 2011).

This study provides an explanation for the observed meridional ammonia anomalies, given the meridionally averaged vertical ammonia profile. The consistency of these results suggest that the T_b latitudinal variations are dominated by the opacity of a passive tracer, rather than the kinetic temperature. Note that evidence for the part of the deep cells extending from 1.5 to 6 bar depends on the flip of the background ammonia gradient (Fig. 2a), and without it these depths might be part of upper inverse cells (Fletcher et al., 2021). The shape of this vertical profile might be set by precipitation, diffusion, and small-scale mixing, all of which might change with latitude and depth (Guillot et al., 2020a). Nonetheless, the remarkable agreement between the model and the data, together with the robust correlation analysis, provide strong evidence that the observed distribution of ammonia is governed by the existence, number, position and relative strength of the Ferrel-like circulation cells in Jupiter.

acknowledgments

All the data used in this study is publicly available, see Tollefson et al. (2017) for the winds data, Salyk et al. (2006) for the eddies data, Li et al. (2017) for the ammonia data, Brown et al. (2018) for the lightning data and Oyafuso et al. (2020) for the brightness temperature data.

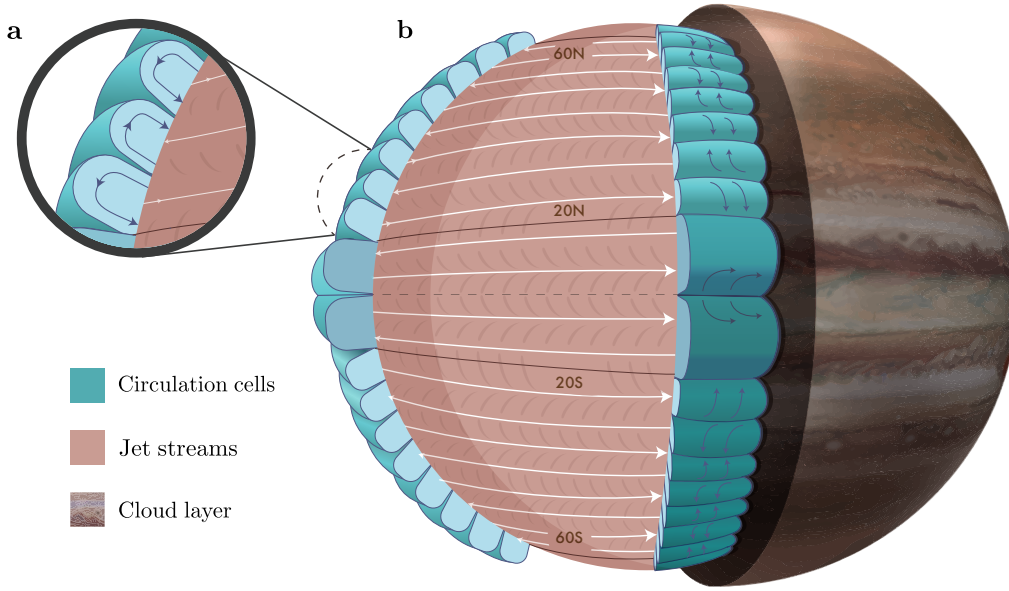


Figure 5: (b) A figurative cross section of Jupiter’s meridional circulation and (a) a magnification of the midlatitude circulation cells. The circulation cells (blue) are axisymmetric in the zonal direction. The pink shell represents a deep layer characteristic for all depths within the circulation cells. The white arrows represent alternating jet streams and are symmetric around the equator for the purpose of clarity. Each jet between latitudes $20^{\circ} - 60^{\circ}$ S/N is accompanied by a turbulence-driven circulation cell (blue arrows) in the meridional plane as illustrated in panel b. The equatorial upwelling associated with the superrotating jet is drawn at the equator, as illustrated in panel e, as part of a larger possible equatorial cell (dark blue).

References

- Aurnou, J. M. and Olson, P. L. (2001). Strong zonal winds from thermal convection in a rotating spherical shell. *Geophys. Res. Lett.*, 28(13):2557–2559.
- Bolton, S. J., Adriani, A., Adumitroaie, V., Allison, M., Anderson, J., Atreya, S., Bloxham, J., Brown, S., Connerney, J. E. P., DeJong, E., Folkner, W., Gautier, D., Grassi, D., Gulkis, S., Guillot, T., Hansen, C., Hubbard, W. B., Iess, L., Ingersoll, A., Janssen, M., Jorgensen, J., Kaspi, Y., Levin, S. M., Li, C., Lunine, J., Miguel, Y., Mura, A., Orton, G., Owen, T., Ravine, M., Smith, E., Steffes, P., Stone, E., Stevenson, D., Thorne, R., Waite, J., Durante, D., Ebert, R. W., Greathouse, T. K., Hue, V., Parisi, M., Szalay, J. R., and Wilson, R. (2017). Jupiter’s interior and deep atmosphere: The initial pole-to-pole passes with the Juno spacecraft. *Science*, 356:821–825.
- Brown, S., Janssen, M., Adumitroaie, V., Atreya, S., Bolton, S., Gulkis, S., Ingersoll, A., Levin, S., Li, C., Li, L., Lunine, J., Misra, S., Orton, G., Steffes, P., Tabataba-Vakili, F., Kolmasova, I., Imai, M., Santolik, O., Kurth, W., Hospodarsky, G., Gurnett, D., and Connerney, J. (2018). Prevalent lightning sferics at 600 megahertz near Jupiter’s poles. *Nature*, 558(7708):87–90.
- Busse, F. H. (1976). A simple model of convection in the Jovian atmosphere. *Icarus*, 29:255–260.
- Busse, F. H. (2002). Convective flows in rapidly rotating spheres and their dynamo action. *Phys. of Fluids.*, 14:1301–1314.
- Christensen, U. R. (2002). Zonal flow driven by strongly supercritical convection in rotating spherical shells. *J. Comp. Phys.*, 470:115–133.
- Christensen, U. R., Wicht, J., and Dietrich, W. (2020). Mechanisms for limiting the depth of zonal winds in the gas giant planets. *Astrophys. J.*, 890(1):61.
- de Pater, I., Dunn, D., Romani, P., and Zahnle, K. (2001). Reconciling Galileo Probe Data and Ground-Based Radio Observations of Ammonia on Jupiter. *Icarus*, 149(1):66–78.

- de Pater, I., Sault, R. J., Wong, M. H., Fletcher, L. N., DeBoer, D., and Butler, B. (2019). Jupiter’s ammonia distribution derived from VLA maps at 3–37 GHz. *Icarus*, 322:168–191.
- Debras, F. and Chabrier, G. (2019). New models of Jupiter in the context of Juno and Galileo. *Astrophys. J.*, 872(1):100.
- Dietrich, W. and Jones, C. A. (2018). Anelastic spherical dynamos with radially variable electrical conductivity. *Icarus*, 305:15–32.
- Duer, K., Galanti, E., and Kaspi, Y. (2020). The range of Jupiter’s flow structures that fit the Juno asymmetric gravity measurements. *J. Geophys. Res. (Planets)*, 125(8).
- Fletcher, L. N., Greathouse, T. K., Orton, G. S., Sinclair, J. A., Giles, R. S., Irwin, P. G., and Encrenaz, T. (2016). Mid-infrared mapping of Jupiter’s temperatures, aerosol opacity and chemical distributions with IRTF/TEXES. *Icarus*, 278:128–161.
- Fletcher, L. N., Kaspi, Y., Guillot, T., and Showman, A. P. (2020). How well do we understand the belt/zone circulation of Giant Planet atmospheres? *Space Sci. Rev.*, 216(2):1–33.
- Fletcher, L. N., Oyafuso, F. A., Allison, M., Ingersoll, A., Li, L., Kaspi, Y., Galanti, E., Wong, M. H., Orton, G. S., Duer, K., Zhang, Z., Li, C., Guillot, T., Levin, S. M., and Bolton, S. (2021). Jupiter’s temperate belt/zone contrasts revealed at depth by Juno microwave observations. *Earth and Space Science Open Archive*, page 35.
- Galanti, E. and Kaspi, Y. (2021). Combined magnetic and gravity measurements probe the deep zonal flows of the gas giants. *Mon. Not. Roy. Astro. Soc.*, 501(2):2352–2362.
- Galanti, E., Kaspi, Y., Duer, K., Fletcher, L. N., Ingersoll, A., Cheng, L., Orton, G. S., Guillot, T., M., L. S., and J., B. S. (2021). Constraints on the latitudinal profile of Jupiter’s deep jets. *Geophys. Res. Lett.*, 48(9):e2021GL092912.
- Garcia-Melendo, E. and Sánchez-Lavega, A. (2001). A study of the stability of jovian zonal winds from HST images: 1995–2000. *Icarus*, 152(2):316–330.
- Gastine, T., Wicht, J., Duarte, L. D. V., Heimpel, M., and Becker, A. (2014). Explaining Jupiter’s magnetic field and equatorial jet dynamics. *Geophys. Res. Lett.*, 41:5410–5419.
- Gierasch, P. J., Magalhaes, J. A., and Conrath, B. J. (1986). Zonal mean properties of Jupiter’s upper troposphere from Voyager infrared observations. *Icarus*, 67:456–483.
- Giles, R. S., Fletcher, L. N., Irwin, P. G., Orton, G. S., and Sinclair, J. A. (2017). Ammonia in Jupiter’s troposphere from high-resolution 5 μm spectroscopy. *Geophys. Res. Lett.*, 44(21):10–838.
- Grassi, D., Adriani, A., Moriconi, M. L., Ignatiev, N. I., D’Aversa, E., Colosimo, F., Negrão, A., Brower, L., Dinelli, B. M., Coradini, A., and Iccioni, G. (2010). Jupiter’s hot spots: Quantitative assessment of the retrieval capabilities of future IR spectro-imagers. *Planetary and Space Science*, 58(10):1265–1278.
- Grassi, D., Adriani, A., Mura, A., Atreya, S. K., Fletcher, L. N., Lunine, J. I., Orton, G. S., Bolton, S., Plainaki, C., Sindoni, G., Altieri, F., Cicchetti, A., Dinelli, B. M., Filacchione, G., Migliorini, A., Moriconi, M. L., Noschese, R., Olivieri, A., Piccioni, G., Sordini, R., Stefani, S., Tosi, F., and Turrini, D. (2020). On the spatial distribution of minor species in Jupiter’s troposphere as inferred from Juno JIRAM data. *J. Geophys. Res. (Planets)*, 125(4).
- Guillot, T., Li, C., Bolton, S. J., Brown, S. T., Ingersoll, A. P., Janssen, M. A., Levin, S. M., Lunine, J. I., Orton, G. S., Steffes, P. G., and Stevenson, D. J. (2020a). Storms and the depletion of ammonia in Jupiter: II. explaining the Juno observations. *J. Geophys. Res. (Planets)*, 125(8):e2020JE006404.
- Guillot, T., Miguel, Y., Militzer, B., Hubbard, W. B., Kaspi, Y., Galanti, E., Cao, H., Helled, R., Wahl, S. M., Iess, L., Folkner, W. M., Stevenson, D. J., Lunine, J. I., Reese, D. R., Biekman, A., Parisi, M., Durante, D., Connerney, J. E. P., Levin, S. M., and Bolton, S. J. (2018). A suppression of differential rotation in Jupiter’s deep interior. *Nature*, 555:227–230.
- Guillot, T., Stevenson, D. J., Atreya, S. K., Bolton, S. J., and Becker, H. N. (2020b). Storms and the depletion of ammonia in Jupiter: I. microphysics of mushballs. *J. Geophys. Res. (Planets)*, 125(8):e2020JE006403.

- Heimpel, M., Aurnou, J., and Wicht, J. (2005). Simulation of equatorial and high-latitude jets on Jupiter in a deep convection model. *Nature*, 438:193–196.
- Iess, L., Folkner, W. M., Durante, D., Parisi, M., Kaspi, Y., Galanti, E., Guillot, T., Hubbard, W. B., Stevenson, D. J., Anderson, J. D., Buccino, D. R., Casajus, L. G., Milani, A., Park, R., Racioppa, P., Serra, D., Tortora, P., Zannoni, M., Cao, H., Helled, R., Lunine, J. I., Miguel, Y., Militzer, B., Wahl, S., Connerney, J. E. P., Levin, S. M., and Bolton, S. J. (2018). Measurement of Jupiter’s asymmetric gravity field. *Nature*, 555(7695):220–222.
- Imamura, T., Mitchell, J., Lebonnois, S., Kaspi, Y., Showman, A. P., and Korabiev, O. (2020). Superrotation in planetary atmospheres. *Space Sci. Rev.*, 216(5):1–41.
- Ingersoll, A. P., Adumitroaie, V., Allison, M. D., Atreya, S., Bellotti, A. A., Bolton, S. J., Brown, S. T., Gulkis, S., Janssen, M. A., Levin, S. M., Cheng, L., Liming, L., Lunine, J. I., Orton, G. S., Oyafuso, F. A., and Steffes, P. G. (2017). Implications of the ammonia distribution on Jupiter from 1 to 100 bars as measured by the Juno microwave radiometer. *Geophys. Res. Lett.*, 44(15):7676–7685.
- Ingersoll, A. P., Atreya, S., Bolton, S. J., Brueschaber, S., Fletcher, L. N., Galanti, E., Kaspi, Y., Levin, S. M., Li, C., Li, L., Lunine, J. I., Orton, G. S., and Waite, H. (2021). Jupiter’s overturning circulation: Breaking waves take the place of solid boundaries. *Geophys. Res. Lett.* in review.
- Ingersoll, A. P., Gierasch, P. J., Banfield, D., Vasavada, A. R., and Galileo Imaging Team (2000). Moist convection as an energy source for the large-scale motions in Jupiter’s atmosphere. *Nature*, 403:630–632.
- Janssen, M. A., Oswald, J. E., Brown, S. T., Gulkis, S., Levin, S. M., Bolton, S. J., Allison, M. D., Atreya, S. K., Gautier, D., Ingersoll, A. P., Lunine, J. I., Orton, G. S., Owen, T. C., Steffes, P. G., Adumitroaie, V., Bellotti, A., Jewell, L. A., Li, C., Li, L., Misra, S., Oyafuso, F. A., Santos-Costa, D., Sarkissian, E., Williamson, R., Arballo, J. K., Kitiyakara, A., Ulloa-Severino, A., Chen, J. C., Maiwald, F. W., Sahakian, A. S., Pingree, P. J., Lee, K. A., Mazer, A. S., Redick, R., Hodges, R. E., Hughes, R. C., Bedrosian, G., Dawson, D. E., Hatch, W. A., Russell, D. S., Chamberlain, N. F., Zawadski, M. S., Khayatian, B., Franklin, B. R., Conley, H. A., Kempenaar, J. G., Loo, M. S., Sunada, E. T., Vorperion, V., and Wang, C. C. (2017). MWR: Microwave Radiometer for the Juno Mission to Jupiter. *Space Sci. Rev.*, 213(1-4):139–185.
- Juckes, M. (2001). A generalization of the transformed Eulerian-mean meridional circulation. *Q. J. R. Meteorol. Soc.*, 127(571):147–160.
- Kaspi, Y., Flierl, G. R., and Showman, A. P. (2009). The deep wind structure of the giant planets: Results from an anelastic general circulation model. *Icarus*, 202:525–542.
- Kaspi, Y., Galanti, E., Hubbard, W. B., Stevenson, D. J., Bolton, S. J., Iess, L., Guillot, T., Bloxham, J., Connerney, J. E. P., Cao, H., Durante, D., Folkner, W. M., Helled, R., Ingersoll, A. P., Levin, S. M., Lunine, J. I., Miguel, Y., Militzer, B., Parisi, M., and Wahl, S. M. (2018). Jupiter’s atmospheric jet-streams extend thousands of kilometres deep. *Nature*, 555:223–226.
- Kaspi, Y., Galanti, E., Showman, A. P., Stevenson, D. J., Guillot, T., Iess, L., and Bolton, S. J. (2020). Comparison of the deep atmospheric dynamics of Jupiter and Saturn in light of the Juno and Cassini gravity measurements. *Space Sci. Rev.*, 216(5):1–27.
- Laraia, A. L. and Schneider, T. (2015). Superrotation in terrestrial atmospheres. *J. Atmos. Sci.*, 72(11):4281–4296.
- Lee, S. and Kaspi, Y. (2021). Towards an understanding of the structure of Jupiter’s atmosphere using the ammonia distribution and the Transformed Eulerian Mean theory. *J. Atmos. Sci.*, 78(7):2047–2056.
- Lewis, S. R., Read, P. L., Conrath, B. J., Pearl, J. C., and Smith, M. D. (2007). Assimilation of thermal emission spectrometer atmospheric data during the Mars Global Surveyor aerobraking period. *Icarus*, 192(2):327–347.
- Li, C., Ingersoll, A., Bolton, S., Levin, S., Janssen, M., Atreya, S., Lunine, J., Steffes, P., Brown, S., Guillot, T., Allison, M., Arballo, J., Bellotti, A., Adumitroaie, V., Gulkis, S., Hodges, A., Li, L., Misra, S., Orton, G., Oyafuso, F., Santos-Costa, D., Waite, H., and Zhang, Z. (2020). The water abundance in Jupiter’s equatorial zone. *Nature Astronomy*, 4(6):609–616.

- Li, C., Ingersoll, A., Janssen, M., Levin, S., Bolton, S., Adumitroaie, V., Allison, M., Arballo, J., Bellotti, A., Brown, S., Ewald, S., Jewell, L., Misra, S., Orton, G., Oyafuso, F., Steffes, P., and Williamson, R. (2017). The distribution of ammonia on Jupiter from a preliminary inversion of Juno microwave radiometer data. *Geophys. Res. Lett.*, 44(11):5317–5325.
- Limaye, S. S. (2007). Venus atmospheric circulation: Known and unknown. *J. Geophys. Res. (Planets)*, 112(E4).
- Little, B., Anger, C. D., Ingersoll, A. P., Vasavada, A. R., Senske, D. A., Breneman, H. H., Borucki, W. J., and Team, T. G. S. (1999). Galileo images of lightning on Jupiter. *Icarus*, 142(2):306–323.
- Liu, J., Goldreich, P. M., and Stevenson, D. J. (2008). Constraints on deep-seated zonal winds inside Jupiter and Saturn. *Icarus*, 196:653–664.
- Liu, J. and Schneider, T. (2010). Mechanisms of jet formation on the giant planets. *J. Atmos. Sci.*, 67:3652–3672.
- Miesch, M. S. and Hindman, B. W. (2011). Gyroscopic pumping in the solar near-surface shear layer. *Astrophys. J.*, 743(1):79.
- Oyafuso, F., Levin, S., Orton, G., Brown, S., Adumitroaie, V., Janssen, M., Wong, M. H., Fletcher, L. N., Steffes, P., Li, C., Gulkis, S., Atreya, S., S., M., and S., B. (2020). Angular dependence and spatial distribution of Jupiter’s centimeter-wave thermal emission from Juno’s microwave radiometer. *Earth Planet. Sci. Lett.*, 7(11):e2020EA001254.
- Porco, C. C., West, R. A., McEwen, A., Del Genio, A. D., Ingersoll, A. P., Thomas, P., Squyres, S., Dones, L., Murray, C. D., Johnson, T. V., Burns, J. A., Brahic, A., Neukum, G., Veverka, J., Barbara, J. M., Denk, T., Evans, M., Ferrier, J. J., Geissler, P., Helfenstein, P., Roatsch, T., Throop, H., Tiscareno, M., and Vasavada, A. R. (2003). Cassini imaging of Jupiter’s atmosphere, satellites and rings. *Science*, 299:1541–1547.
- Potter, S. F., Vallis, G. K., and Mitchell, J. L. (2014). Spontaneous superrotation and the role of Kelvin waves in an idealized dry GCM. *J. Atmos. Sci.*, 71(2):596–614.
- Read, P. L., Lewis, S. R., and Vallis, G. K. (2018). Atmospheric dynamics of terrestrial planets. *Handbook of Exoplanets*, 144:2537–2557.
- Salyk, C., Ingersoll, A. P., Lorre, J., Vasavada, A., and Del Genio, A. D. (2006). Interaction between eddies and mean flow in Jupiter’s atmosphere: Analysis of Cassini imaging data. *Icarus*, 185:430–442.
- Schneider, T. (2006). The general circulation of the atmosphere. *Ann. Rev. Earth Plan. Sci.*, 34:655–688.
- Schneider, T. and Liu, J. (2009). Formation of jets and equatorial superrotation on Jupiter. *J. Atmos. Sci.*, 66:579–601.
- Showman, A. P. and de Pater, I. (2005). Dynamical implications of Jupiter’s tropospheric ammonia abundance. *Icarus*, 174:192–204.
- Taylor, F. W., Atreya, S. K., Encrenaz, T. H., Hunten, D. M., Irwin, P. G., and Owen, T. C. (2004). *Jupiter: the planet, satellites and magnetosphere*, chapter The composition of the atmosphere of Jupiter, pages 59–78. Cambridge University Press.
- Tollefson, J., Wong, M. H., de Pater, I., Simon, A. A., Orton, G. S., Rogers, J. H., Atreya, S. K., C., R. G., Januszewski, W., Morales-Juberías, R., and S., M. P. (2017). Changes in Jupiter’s zonal wind profile preceding and during the Juno mission. *Icarus*, 296:163–178.
- Vallis, G. K. (2017). *Atmospheric and Oceanic Fluid Dynamics*. pp. 770. Cambridge University Press., second edition.
- Vasavada, A. R. and Showman, A. P. (2005). Jovian atmospheric dynamics: An update after Galileo and Cassini. *Reports of Progress in Physics*, 68:1935–1996.
- Wicht, J. and Gastine, T. (2020). Numerical simulations help revealing the dynamics underneath the clouds of Jupiter. *Nature Communications*, 11(1):1–4.
- Wicht, J., Gastine, T., Duarte, L. D., and Dietrich, W. (2019). Dynamo action of the zonal winds in Jupiter. *Astron. and Astrophys.*, 629:A125.

- Young, R. M. and Read, P. L. (2017). Forward and inverse kinetic energy cascades in Jupiter’s turbulent weather layer. *Nature Physics*, 13(11):1135–1140.
- Young, R. M., Read, P. L., and Wang, Y. (2019). Simulating Jupiter’s weather layer. Part I: Jet spin-up in a dry atmosphere. *Icarus*, 326:225–252.

Supporting Information

S1 Eddy momentum driven Ferrel-like cell

S1.1 Standard formulation

Using approximations similar to the commonly used formulation which describe the terrestrial Ferrel-cell dynamics (Vallis, 2017), the leading order zonal mean zonal momentum equation may be written as

$$\frac{\partial \bar{u}}{\partial t} + \frac{\partial}{\partial y} (\overline{u'v'}) - f\bar{v} = -F_{\text{sink}}, \quad (\text{S1})$$

where F_{sink} is a sink term. On Earth, the sink term represents a surface drag in the Ekman layer and in the Jovian atmosphere, if the cells are as deep as the jets (Kaspi et al., 2020), it might be Ohmic dissipation (Liu et al., 2008; Liu and Schneider, 2010; Kaspi et al., 2020) (i.e., $F_{\text{sink}} = \frac{1}{4\pi\rho} (\nabla \times \mathbf{B}) \times \mathbf{B}$, where \mathbf{B} is the 3D magnetic field and ρ is density). Eq. 1¹, adequate for the upper branch of the cells, results from applying time-averaging away from the sink layer. This balance leads to meridional velocities in the directions illustrated in Fig. 2b². Alternatively, applying vertical integration cancels the Coriolis terms in the vertical boundaries of the cell and the relation between the zonal jets, their eddy source term and the sink term becomes

$$\frac{\partial \bar{U}}{\partial t} = -\frac{\partial}{\partial y} (\overline{U'V'}) - \hat{F}_{\text{sink}}. \quad (\text{S2})$$

where U and V are the vertically integrated velocities, and \hat{F}_{sink} is the vertically integrated sink term. Therefore, converging (diverging) eddy momentum fluxes transfer their momentum to eastward (westward) jets, as can be seen in the Jovian atmosphere (Fig. 1b,d). In the descriptions throughout this study, Cartesian approximations are used for the sake of clarity, but the actual calculations were performed using the spherical, more accurate, formulations.

S1.2 TEM formulation for Jupiter

The Transformed Eulerian Mean (TEM) equations, commonly invoked to quantify Lagrangian mass-transport in Earth’s Ferrel cells, describe a circulation driven by the diabatic heating term (Vallis, 2017). The TEM formulation can be derived from the momentum and thermodynamic equations, under Boussinesq and quasi-geostrophic approximations (Vallis (2017), ch. 10.3), resulting in

$$\frac{\partial \bar{u}}{\partial t} - f\bar{v}^* = \nabla \cdot \mathcal{F}, \quad (\text{S3})$$

and

$$\frac{\partial \bar{b}}{\partial t} - \bar{w}^* N^2 = \bar{S}, \quad (\text{S4})$$

where $\bar{v}^* = \bar{v} - \frac{\partial}{\partial z} (\frac{1}{N^2} \overline{v'b'})$ and $\bar{w}^* = \bar{w} + \frac{\partial}{\partial y} (\frac{1}{N^2} \overline{v'b'})$ are defined as the “residual” mean meridional and vertical velocities, respectively, which approximate mass-transport by both Eulerian mean velocities and eddy fluxes, $N^2 = \partial \bar{b}_0 / \partial z$ is the Brunt-Vaisala frequency, \bar{S} is the diabatic heating term, and $\mathcal{F} = -(u'v')\hat{j} + (\frac{f}{N^2} \overline{v'b'})\hat{k}$ is the Eliassen-Plam (EP) flux. b_0 and b represent the mean (zonally- and meridionally-averaged) and the deviation from the mean of the buoyancy force and \hat{j} (\hat{k}) is a unit vectors in the meridional (vertical) direction. On Earth, the diabatic heating term is important (Vallis, 2017), and therefore the residual meridional velocities accurately represent the total meridional transport of mass in Earth’s midlatitudes.

The midlatitude atmosphere on Earth is characterized by baroclinicity, and as a result, the second term of the EP flux is substantial and plays a key role in the resulting circulation. On Jupiter, the eddy fluxes beneath the cloud level and the diabatic heating are yet to be measured. However, gravity-measurement analysis implies that Jupiter’s jets are nearly barotropic in the depth range relevant to this study (Galanti and Kaspi, 2021), meaning that the EP flux is dominated by the first term, and \bar{w}^* is comparable to \bar{w} (Lee and Kaspi, 2021). Therefore, under the barotropic limit, the equations describing the Eulerian velocities in a Ferrel-like cell might also represent the total mass transport in the Jovian cells.

¹Note that equation cross-references without a S refer to equations in the main text.

²Note that figure cross-references without a S refer to figures in the main text.

S1.3 Correlation analysis

The picture illustrated in Fig. 2, relating the distribution of ammonia and the zonal winds according to the Ferrel-like cells hypothesis, is tested quantitatively in a correlation analysis exhibited in Fig. 3. The expected relations between the zonal jets and the ammonia meridional gradients in the NH are

$$\bar{u} \propto \begin{cases} -\partial_y m_a & 1.5 \leq p < 6 \text{ bar} \quad (\text{channels 4 - 5}), \\ \partial_y m_a & p \geq 6 \text{ bar} \quad (\text{channels 1 - 3}), p < 1.5 \text{ bar} \quad (\text{channel 6}). \end{cases} \quad (\text{S5})$$

Here, $\partial_y m_a$ is the latitudinal gradient of the ammonia concentration (m_a) and p is pressure. The channels refer to the six frequencies of Juno's MWR. In the SH, as the circulation is reversed, Eq. S5 flips signs. Eq. S5 captures also the case of cells with westward jets, as both \bar{u} and $\partial_y m_a$ change sign. A Pearson correlation coefficient ($S(\vartheta, \text{ch})$) is calculated for each latitude and MWR channel, and its value is represented by a color between blue, representing a negative correlation, white, representing no correlation and red, representing a positive correlation. The T_b data is measured in a resolution of $\sim 0.6^\circ$ latitude. The data is interpolated such that the grid size is 0.1° latitude, and the correlation for each point ϑ_i is calculated along a span $\{\vartheta_i - 2^\circ, \vartheta_i + 2^\circ\}$. This choice of a 4° latitudinal bin allows having enough data points for the statistical value of the correlation (more than 6 data pairs), and ensures the local nature of the results. The correlations on the MWR data are calculated between the following trends. In Fig. 3a, channels 1-3 and 6 and in Fig. 3c channels 4-5 the color represents the correlation $\bar{u} \propto \partial_y T_b$. In Fig. 3a, channels 4-5 and in Fig. 3c channels 1-3 and 6 the color represents the correlation $\bar{u} \propto -\partial_y T_b$. Note that anomalies of brightness temperature and ammonia abundance are inversely proportional (Li et al., 2017). In Fig. 3b the correlations at all channels are calculated according to $\bar{u} \propto -T_b$. Here, T_b is the Nadir component of the brightness temperature [°K] (other emission angles were not included in the analysis), averaged over nine Juno orbits (PJs 1, 3, 4, 5, 6, 7, 8, 9 and 12) (Oyafuso et al., 2020). For further discussion regarding limb-darkening T_b we point the readers to Fletcher et al. (2021). \bar{u} is Jupiter's zonally-averaged zonal wind [m s^{-1}] measured by the Hubble space telescope during Juno's third perijove (Tollefson et al., 2017), projected barotropically along the axis of rotation (Galanti and Kaspi, 2021; Galanti et al., 2021). The ammonia distribution by JIRAM is estimated at a depth of ~ 6 bar, which is the depth where a local minimum appears in M_a (Fig. 2a). Arbitrarily, the correlation is performed according to $p > 6$ bar in Eq. 2 (Fig. 2d) and the overall positive result points that indeed the depth level of JIRAM measurements should be deeper than the local minimum of M_a . The ammonia estimates from JIRAM are measured in a resolution of 1° latitude. Similar to the T_b correlation analysis, the data is interpolated, and the correlation is performed on a 4° latitude bin for consistency. In Fig. 3d (f) the color represents the correlation $\bar{u} \propto -\partial_y m_a$ ($\bar{u} \propto \partial_y m_a$) and in Fig. 3e the color represents the correlation $\bar{u} \propto m_a$. Finally, the eddy momentum flux convergence is measured in a resolution of 1° latitude, and the correlation is performed using the same latitudinal bin of 4° . In Fig. 3g (h) the color represents the correlation $\bar{u} \propto -\partial_y (u'v')$ ($\bar{u} \propto \partial_y (u'v')$).

We also examine the correlation between the zonal wind and the lightning gradient. We find a good match in the northern hemisphere and a weak negative correlation in the southern hemisphere, where Juno is much less sensitive to lightnings (Fig. S1). Note that the correlation between lightnings and the Ferrel cells is less indicative, as we should only examine the correlation in the rising branch of the cells. Therefore, the correlation values away from the rising branch should be regarded with caution.

S1.4 Advection-relaxation model

S1.4.1 T_b as an indicator for ammonia

As ammonia estimates by Juno's MWR for the high midlatitudes are not yet available, we express the T_b measurements as ammonia in order to examine the model results. For that, we define a reconstructed ammonia distribution from Juno MWR data ($m_a^{\text{(data)}}$), used as a benchmark for the advection-relaxation model, constructed by the mean ammonia calculated from MWR measurements of PJ1 (M_a , Fig. 2a) (Li et al., 2017) and T_b measurements averaged over multiple Juno orbits (PJs 1-12) (Oyafuso et al., 2020). The standard deviation between the perijoves is computed as a function of latitude to validate that the latitudinal variations appearing in the T_b data are physical (Fig. S3 for the midlatitudes and Fig. S4 for the equatorial region). We estimate the T_b anomalies (T'_b) by removing the cross-channel average ($T_{b,\text{mean}}(\text{ch})$) from each MWR channel, and then decompose T'_b into Legendre polynomials and reconstruct the anomalies without the low polynomials to remove large scale variations. These variations, representing equator to pole radiation differences, are not related to ammonia variations by meridional cells (Oyafuso et al., 2020). The reconstructed ammonia is then

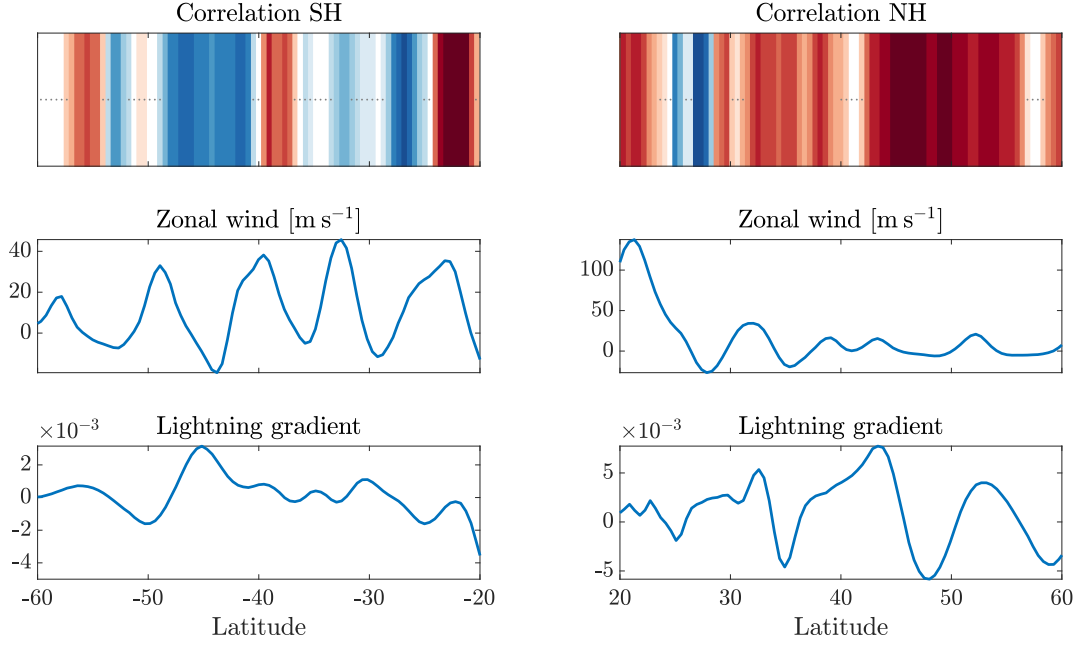


Figure S1: Correlation coefficients (upper panels) between the zonal wind (middle panels) and the lightning meridional gradient (lower panels) in the midlatitudes.

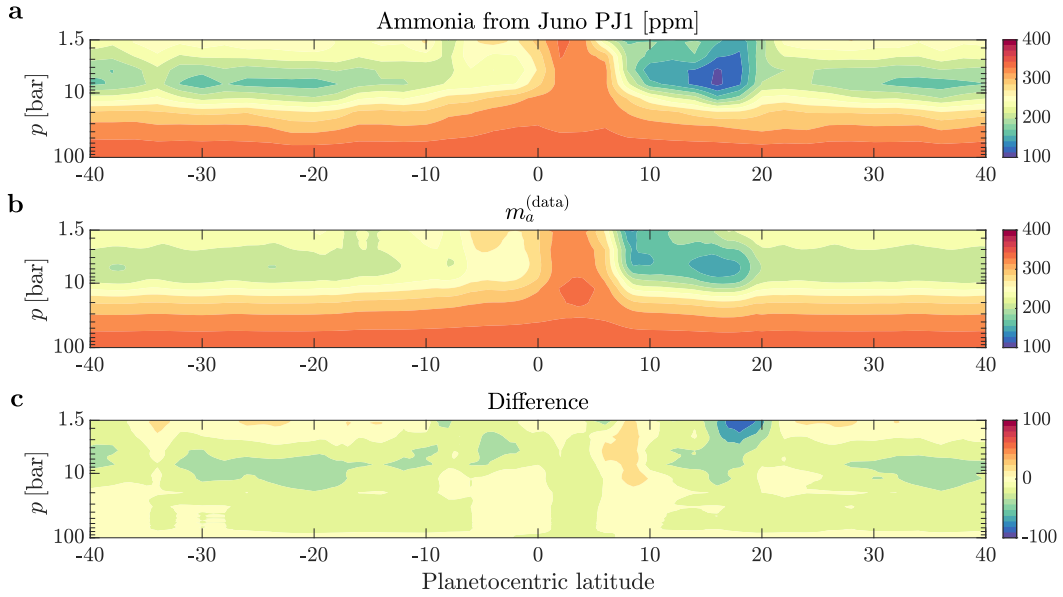


Figure S2: (a) Ammonia estimate (Li et al., 2017) from Juno MWR PJ1 data. (b) m_a calculated from T_b (Eq. S8). This field is used as a benchmark ($m_a^{(\text{data})}$) for the model results. (c) the difference between panel a and panel b.

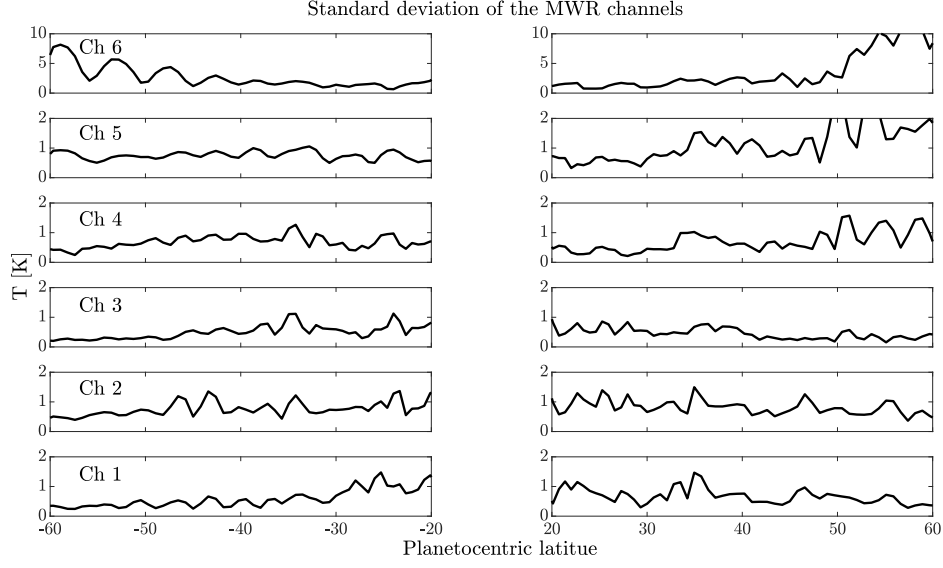


Figure S3: The standard deviation (STD) of the nadir T_b in the midlatitudes computed from nine different perijoves through PJs 1-12 (Oyafuso et al., 2020), in the six MWR channels. The STD is computed after the trend removal for each perijove, as detailed in eq. S7. For channels 1-5, the STD values are smaller than the variation seen in the data (Fig. 1h). Note that although the STD values for channel 6 are higher, at some latitudes, than the mean latitudinal variation (of the same channel), this channel senses at altitudes which are above the cells identified in this study.

$$T'_b(\vartheta, \text{ch}) = T_b(\vartheta, \text{ch}) - T_{b, \text{mean}}(\text{ch}) \cong \sum_{i=1}^N A_i(\vartheta, \text{ch}) P_i(\sin \vartheta), \quad (\text{S6})$$

$$T'_{b, \text{rec}}(\vartheta, \text{ch}) = \sum_{i=30}^N A_i(\vartheta, \text{ch}) P_i(\sin \vartheta), \quad (\text{S7})$$

$$m_a^{(\text{data})}(\vartheta, \text{ch}) = M_a(\text{ch}) - K(\text{ch}) T'_{b, \text{rec}}(\vartheta, \text{ch}), \quad (\text{S8})$$

where P_i are the Legendre polynomials, A_i are the associated coefficients, $N = 200$ is the number of polynomials used and K [ppm · degrees⁻¹] is a depth-dependent 'key', optimized at each depth using Matlab's 'fmincon' to best fit the estimated ammonia distribution from PJ1 (Li et al., 2017). Note that T_b is available between latitudes 90°S to 90°N, therefore $P_{i=30}$ is equivalent to a wavelength of approximately 12° latitude. As the jets widths are not larger the 8° in latitude, this truncation removes variations that are not due to the existence of meridional Ferrel-like cells. The overall structure of $m_a^{(\text{data})}$ is very similar to the ammonia map from PJ1 (Li et al., 2017), while the meridional anomalies now represent well PJs 1-12 (Fig. S2). Finally, the resulting K ranges between 5 at 1 bar to 0 at depth and is used to estimate $m_a^{(\text{data})}$ at latitudes 60°S to 60°N. The profile is interpolated between 1 and 240 bar, according to the relevant pressure levels of each channel (Fig. 4d). These levels are estimated according to the peak of the contribution function of each MWR channel, to give that channels {1, 2, 3, 4, 5, 6} correspond to pressure levels of {240, 30, 9, 3, 1.5, 0.7} bar (Janssen et al., 2017; Bolton et al., 2017).

S1.4.2 Cells construction and parameterization

To describe the meridional cells in the simplest manner, we parameterize each cell (indexed k) with an ellipse, according to a parameter l_k as follows

$$l_k = \sqrt{\frac{(d-a)^2}{a^2} + \frac{(\vartheta - \vartheta_k)^2}{b_k^2}}. \quad (\text{S9})$$

Here, d is defined as downward distance from the cloud level, and a and b_k are the vertical and meridional extents of the cell, respectively. ϑ_k is the latitude of the center of cell k (black dots in Fig. S5a,b). b_k is set according to half the width of cell k (the distance between a black line and a black dot in Fig. S5a,b). The outline of cell k

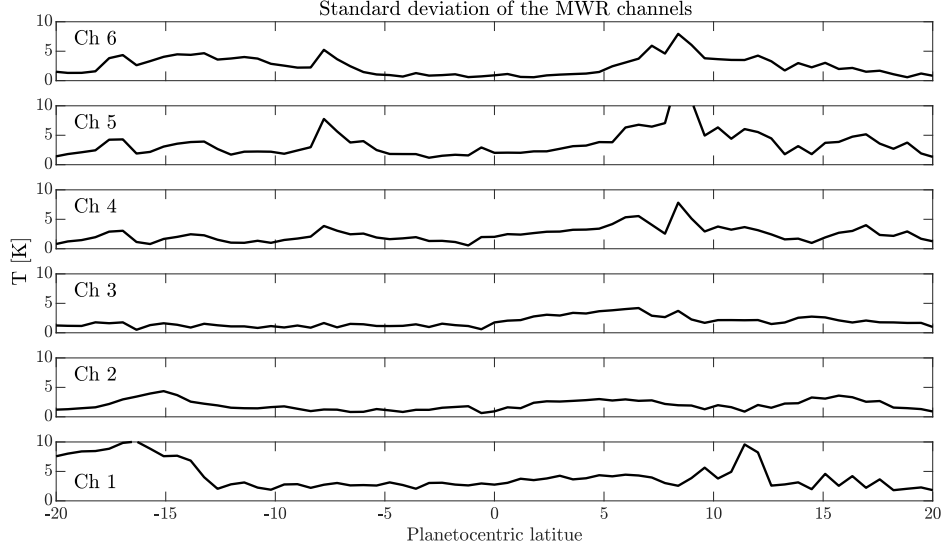


Figure S4: The equatorial standard deviation of the nadir T_b computed from nine different perijoves through PJs 1-12 (Oyafuso et al., 2020), in the six MWR channels. The STD is computed on the original nadir coefficients.

(representing the path of the peak tangential velocity along the cell) is thereby defined by $l_k = 1$. For simplicity, the velocities in a cell are defined using a normal distribution according to

$$\begin{aligned} v_k &= V_k \exp \left[-\frac{1}{2} \left(\frac{l_k - 1}{\tilde{\sigma}} \right)^2 \right] \sin \phi, \\ w_k &= V_k \exp \left[-\frac{1}{2} \left(\frac{l_k - 1}{\tilde{\sigma}} \right)^2 \right] \cos \phi, \\ \tilde{\sigma} &= \sigma \left(\cos^2 \vartheta + \frac{b_k}{a} \sin^2 \vartheta \right), \end{aligned} \quad (\text{S10})$$

where $\phi = \arctan \left[\frac{d-a}{R_J \sin(\vartheta - \vartheta_k)} \right]$, R_J is Jupiter's radius and σ is a parameter for the broadness of a cell's branch. V_k represents the relative strength (velocity) of cell k , parameterized according to the square root of the averaged eddy momentum flux convergence within the cell (Fig. S5b), and its sign represents the cell's direction (clockwise/counter-clockwise), set according to the zonal wind sign at the center of the cell (Fig. S5a).

S1.4.3 Optimization and numerical solution

To solve for m_a , Eq. 3 is discretized using finite differences as

$$\bar{w}_{i,j} \frac{m_{i-1,j} - m_{i+1,j}}{2dr} + \bar{v}_{i,j} \frac{m_{i,j+1} - m_{i,j-1}}{2R_J d\vartheta} = -G_i (m_{i,j} - M_i), \quad (\text{S11})$$

where the “a” subscript of m and M was removed for clarity. Here i , and j are indices for the grid points in the r and ϑ directions, respectively. dr and $d\vartheta$ are the distances between adjacent points in each direction. Eq. S11 constitutes one of n^2 equations for n^2 variables, where n is the resolution of the grid in each direction. Eq. S11 is rearranged in a matrix form as $Ax = b$ such that m_a can be calculated from $A^{-1}b$.

The parameters G_i , σ and a are unknowns. For this, the Matlab optimization function 'fmincon' is used for deciding G_i , σ and a to best reproduce the $m_a^{(\text{data})}$ map. The cost function

$$f(G, \sigma, a) = \sum_{i,j} \left(\left| m_{i,j}^{(\text{model})} - m_{i,j}^{(\text{data})} \right| \right)^2 \quad (\text{S12})$$

is the measure used to find the optimal parameters. The resulting value of G is shown in Fig. S6 for the case of G that is varying with depth, and for comparison, the solution with a constant G is shown as well. The value of σ was found to be ~ 0.85 in both cases. The parameter a was found to be ~ 1600 bar.

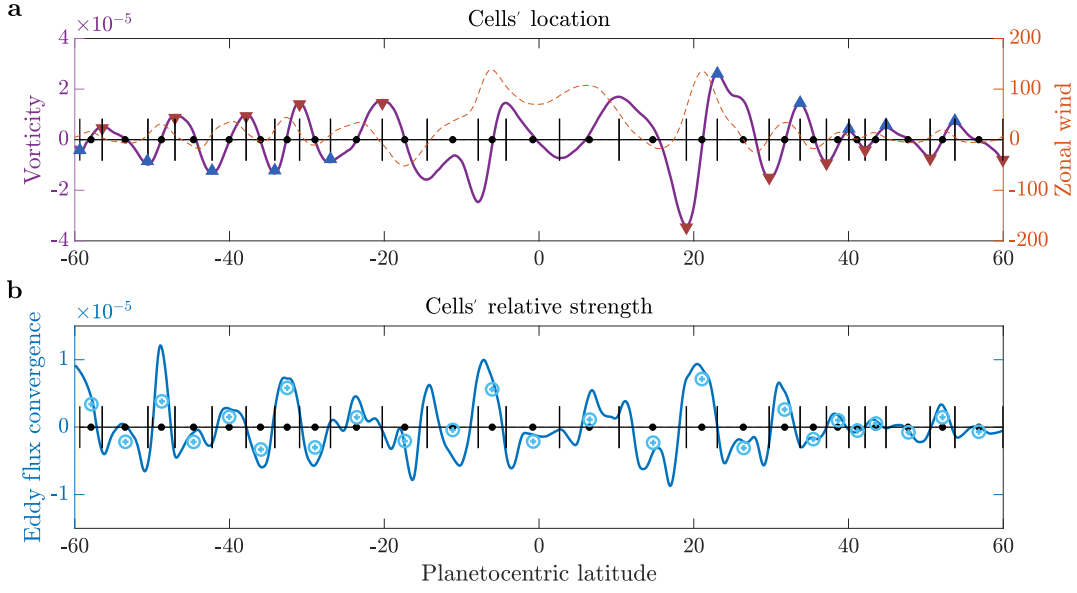


Figure S5: (a) Vorticity (purple) and zonal wind (dashed, orange). Blue (red) triangles represent vorticity peaks ($\partial\zeta/\partial y = 0$), where the vertical branches of the cells drive upward (downward) motion. The cells' centers are positioned between vorticity peaks (black dots), and the cells' extents ($2b_k$) are the distances between pairs of black lines. (b) Eddy momentum flux convergence (blue) and the cells' location as in panel a. Cells' relative strength is set by the averaged value of eddy flux convergence within the cell (light blue circles).

S1.4.4 Robustness analysis

To validate that the model results are robust and not sensitive to the specific parameters found by the optimization analysis, $m_{i,j}^{(\text{model})}$ was also solved from equation 3 using a chosen set of parameters instead of the optimized set. The depth of the cells was chosen to be 3000 km ($a = 1500$ km), in accordance with the depth of the jets that was estimated from gravity measurements (Kaspi et al., 2018). The width of the cells was chosen such that one standard deviation covers half a cell's width ($\sigma = 0.5$). G is degenerated into a constant (no dependence in z) and is set, from a scaling argument, as $G = \max(w)/a$ [s^{-1}]. As seen in the results (Fig. S7), the modeled ammonia anomalies map still predicts the data convincingly. The main difference is the depth where the sign of the ammonia anomalies flip (between 3 and 6 bar), which is now only controlled by the input M_a (Li et al., 2017), and could not be 'corrected' by a depth-dependent relaxation time scale. It can be seen that the essence of the circulation cells is still very apparent in the results.

S2 Equatorial region analysis

S2.1 Estimate for the extent of the equatorial region

The tangent cylinder is the projection (along the axis of rotation) of the planet's solid-body rotating core on the outer shell. The equatorial latitudes lie outside of the tangent cylinder, and is thereby characterized by a different dynamical regime than that of the midlatitudes. To separate quantitatively the midlatitudes, positioned within the tangent cylinder, from the equatorial region, it is required to know the depth of the atmosphere (D_{atm}) and the radius of the planet (R). The latitudes of the cylinder's edge (α) can then be derived from geometrical considerations as

$$\alpha = \arccos\left(1 - \frac{D_{\text{atm}}}{R}\right). \quad (\text{S13})$$

Gravity analysis reveals that Jupiter's atmosphere is approximately 3000 km deep (Guillot et al., 2018; Kaspi et al., 2018). Substituting $D_{\text{atm}} = 3000$ km and $R = R_J = 70,000$ km in Eq. S13 gives $\alpha = \pm 16.8^\circ$. This means that fluid columns parallel to the axis of rotation in the latitude range $-17^\circ \leq \vartheta \leq 17^\circ$, can theoretically extend uninterruptedly between the hemispheres.

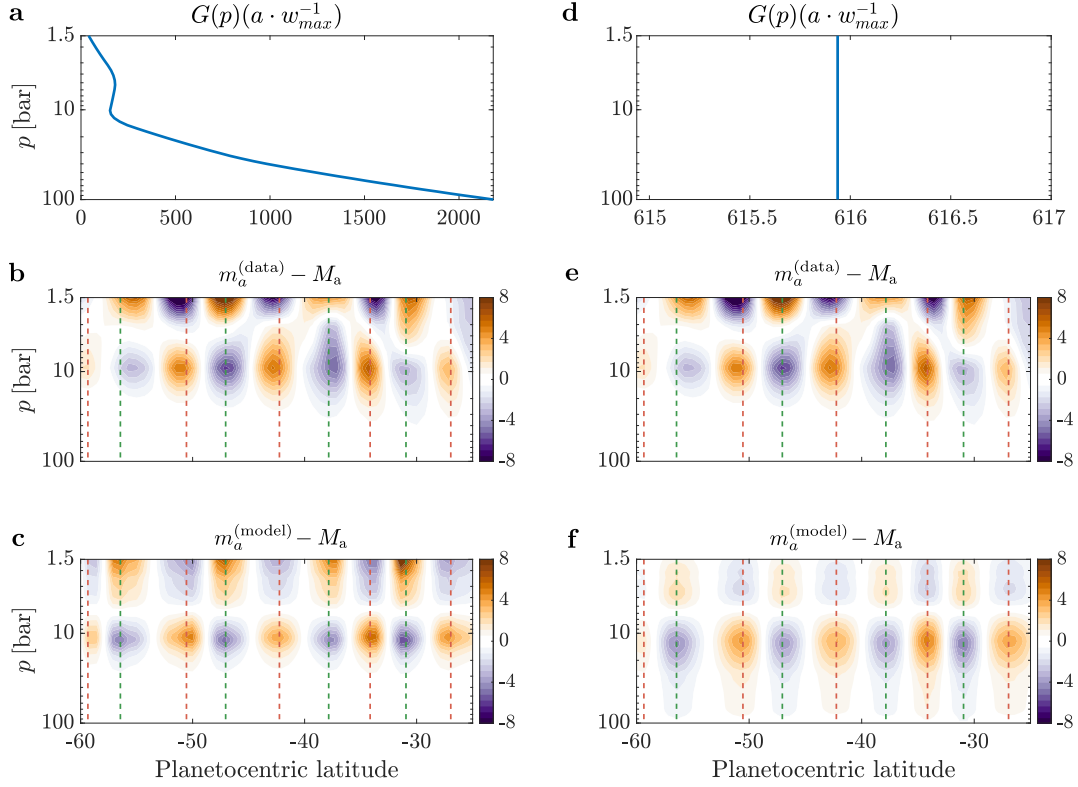


Figure S6: Comparison between model results with and without vertical variation in G . (a) The vertical variation of the normalized source term G used for Fig. 4c. (b and e), $m_a^{(\text{data})}$ anomalies [ppm] in the SH. (c) The ammonia anomalies [ppm] map produced by the advection-relaxation model with the source term from panel a. (d) Constant normalized source term G in Eq. 3. (f) The ammonia anomalies [ppm] map produced by the advection-relaxation model with the source term from panel d. In panels b, c, e and f the vertical mean profile M_a is removed from the ammonia map m_a and dashed red and green lines are the upward and downward branches of the cells, respectively. The comparison reveals that although the solution with varying source term (a) results in a better model solution (c) compared to the measurements (b and d), the essence of the anomalies (f) is well captured with a constant source term (d).

S2.2 Theory for the leading balance in the Jovian equatorial region

Starting from the primitive equations (Vallis, 2017), the continuity and zonal momentum equations in spherical coordinates are

$$\frac{\partial \rho}{\partial t} + \rho \left(\frac{1}{R_J \cos \vartheta} \frac{\partial u}{\partial \lambda} + \frac{1}{R_J \cos \vartheta} \frac{\partial}{\partial \vartheta} (v \cos \vartheta) + \frac{\partial w}{\partial r} \right) + \frac{u}{R_J \cos \vartheta} \frac{\partial \rho}{\partial \lambda} + \frac{v}{R_J} \frac{\partial \rho}{\partial \vartheta} + w \frac{\partial \rho}{\partial r} = 0, \quad (\text{S14})$$

and

$$\frac{\partial u}{\partial t} + \frac{u}{R_J \cos \vartheta} \frac{\partial u}{\partial \lambda} + \frac{v}{R_J} \frac{\partial u}{\partial \vartheta} + w \frac{\partial u}{\partial r} - 2\Omega (\sin \vartheta v - \cos \vartheta w) - \frac{uv}{R_J} \tan \vartheta = -\frac{1}{R_J \rho \cos \vartheta} \frac{\partial p}{\partial \lambda}, \quad (\text{S15})$$

respectively, where λ is longitude. The mean density (ρ_m) is assumed to only change with r , and anomalies from it are assumed to be much smaller than the mean value. In addition, the meridional derivatives and the meridional velocity are assumed very small near the equator, relative to the other terms. This assumption is based on the symmetry around the equator. Assuming also a steady state, Eq. S14 and Eq. S15, evaluated on the equatorial plane ($\vartheta = 0^\circ$), are then

$$\rho_m \left(\frac{1}{R_J} \frac{\partial u}{\partial \lambda} + \frac{\partial w}{\partial r} \right) + w \frac{\partial \rho_m}{\partial r} = 0, \quad (\text{S16})$$

and

$$\frac{u}{R_J} \frac{\partial u}{\partial \lambda} + w \frac{\partial u}{\partial r} + 2\Omega w = -\frac{1}{R_J \rho_m} \frac{\partial p}{\partial \lambda}. \quad (\text{S17})$$

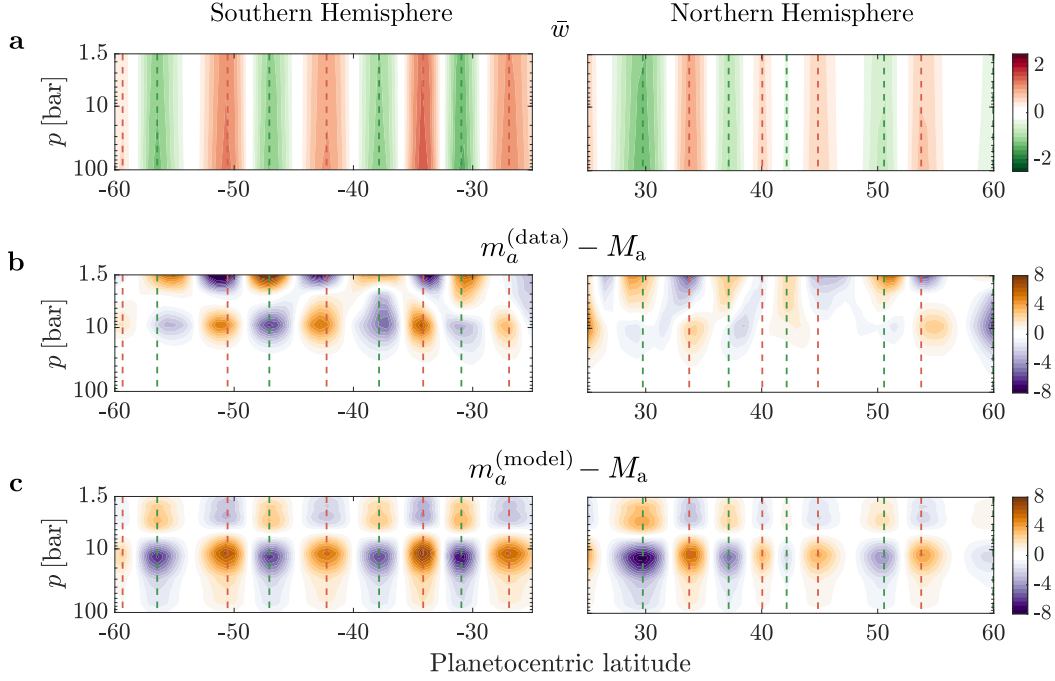


Figure S7: Model robustness analysis. An example for a model run without optimization. The optimized variables in this run are set manually according to physical considerations. The depth of the cells (a) is set to 1,500 km such that the cells extend 3,000 km in accordance with gravity measurements for the depth of the zonal jets (Kaspi et al., 2018). The relaxation constant G is set (without height dependence) from scaling argument by equating the relaxation term in equation 3 to the vertical advection term, leading to $G = \max(w)/a$. The value of σ is set to 0.5. (a) The normalized vertical velocity as a function of latitude and pressure. (b) The ammonia anomalies map that was reconstructed from Juno’s MWR measurements. (c) The map of ammonia anomalies resultant from the degenerated model. It can be seen that the optimization procedure doesn’t change the nature of the results which is robust. The structure of the anomalies stays largely the same both in this figure and in Fig. 4, and it stems mostly from the latitudinal structure of the wind and the vertical stratification of the ammonia, both being derived from observations.

Eq. S17 can equivalently be represented as

$$\frac{1}{R_J} \frac{\partial u^2}{\partial \lambda} + \frac{1}{\rho_m} \frac{\partial (w u \rho_m)}{\partial r} - \frac{u}{\rho_m} \left(\rho_m \frac{1}{R_J} \frac{\partial u}{\partial \lambda} + \rho_m \frac{\partial w}{\partial r} + w \frac{\partial \rho_m}{\partial r} \right) + 2\Omega w = -\frac{1}{R_J \rho_m} \frac{\partial p}{\partial \lambda}, \quad (\text{S18})$$

where the third term vanishes according to Eq. S16. Next, the velocities are decomposed via Reynolds decomposition ($u = u' + \bar{u}$, $w = w' + \bar{w}$), such that the zonal mean of Eq. S18 gives

$$-\frac{\partial (\overline{w' u' \rho_m})}{\partial r} = \bar{w} \frac{\partial (\bar{u} \rho_m)}{\partial r} + 2\rho_m \Omega \bar{w} + \rho_m \bar{u} \frac{\partial \bar{w}}{\partial r}. \quad (\text{S19})$$

This shows that the momentum originating from the eddy momentum flux convergence $\left(\frac{\partial (\overline{w' u' \rho_m})}{\partial r} < 0 \right)$, which drives the equatorial superrotation (Kaspi et al., 2009), is divided between the growing equatorial super-rotating jet $\left(\frac{\partial (\bar{u} \rho_m)}{\partial r} > 0, \bar{u} > 0 \right)$, the Coriolis force and another residual term. The growing equatorial jet has been shown in many numerical simulations of superrotation (Heimpel et al., 2005; Kaspi et al., 2009; Gastine et al., 2014). It is a good assumption that each of the terms on the right side is of smaller magnitude than the source term on the left side. Finally, rearranging Eq. S19 gives

$$\bar{w} = -\frac{1}{\underbrace{\frac{\partial (\bar{u} \rho_m)}{\partial r}}_{>0} + \underbrace{2\rho_m \Omega}_{>0}} \underbrace{\left(\frac{\partial (\overline{w' u' \rho_m})}{\partial r} + \rho_m \bar{u} \frac{\partial \bar{w}}{\partial r} \right)}_{<0} > 0. \quad (\text{S20})$$

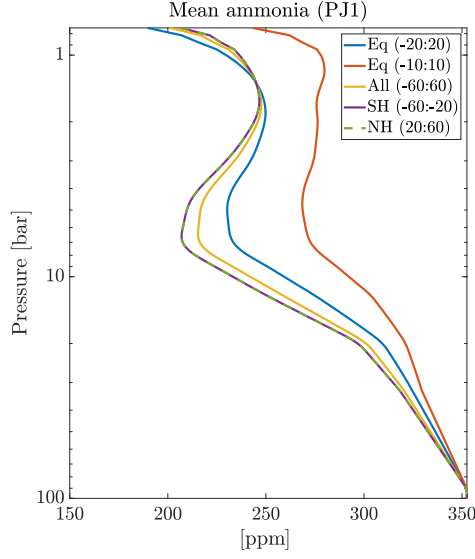


Figure S8: Meridional averaged ammonia values at different latitudinal regions. The lines are calculated according to the inferred ammonia map from PJ1 (Li et al., 2017). Each line is averaged at the latitudinal range described in the legend.

To further simplify, Eq. S20 can be shown for the case of small Rossby number:

$$\bar{w} = -\frac{1}{2\rho_m\Omega} \frac{\partial (\overline{w'u'}\rho_m)}{\partial r} > 0. \quad (\text{S21})$$

This implies that the mean upwelling (\bar{w}) correlates with eddy momentum flux convergence, and therefore with the equatorial superrotating jet at the equatorial region. Since the superrotating jet is supposed to be driven by angular momentum fluxes in the direction perpendicular to the rotation axis (Heimpel et al., 2005; Kaspi et al., 2009; Schneider and Liu, 2009), converging in the equatorial region, Eq. S21 would take the more general form

$$\bar{w}_\perp = -\frac{1}{2\rho_m\Omega} \partial_\perp (\overline{w'_\perp u'}\rho_m) > 0, \quad (\text{S22})$$

where w_\perp and ∂_\perp are the velocity and the gradient in the direction perpendicular to the axis of rotation, i.e., $w_\perp = w \cos \vartheta + v \sin \vartheta$ and $\partial_\perp = (\cos \vartheta) \partial_r + (r^{-1} \sin \vartheta) \partial_\vartheta$.